Density equilibration near the liquid-vapor critical point of a pure fluid: Single phase $T > T_c$

Fang Zhong and Horst Meyer
Department of Physics, Duke University, Durham, North Carolina 27708-0305
(Received 17 November 1994)

A systematic study is reported, both experimental and theoretical, on the density equilibration in a pure fluid, ^{3}He, near the liquid-vapor critical point. Measurements of the density ρ were carried out with capacitive sensors located in the upper and the lower half of a flat horizontal cell. The density change $\delta\rho(t)$ after a step change in temperature of the cell walls was recorded along the critical isochore and along several isotherms above the critical temperature T_c. Direct observation of the sharp response from adiabatic energy transfer into the bulk fluid ("piston effect") is reported. The $\delta\rho(t)$ transients also show the effect from the stratification change, and the relaxation time of the equilibration process is found to diverge and then tend to a constant value as T_c is approached. The entropy transport equation is solved numerically in one dimension for ^{3}He in the critical region above T_c and in the approximation of negligible mass flow velocity and instantaneous local hydrostatic equilibrium. The predictions for the temporal and spatial evolution of temperature, pressure, and density of the fluid layer following a temperature step of the enclosure are presented. The predictions for the profile $\delta\rho(t)$ are compared with the experimental results and show good agreement in shape and amplitude, but a difference in time scale. The approximations in the theory and the geometry of the cell are discussed. Predictions are also made for the equilibration under reduced gravity along the critical isochore, and the fluid steady-state rms density deviation $\langle \delta\rho^2 \rangle^{1/2}$ is computed for two temperature ramping rates at zero gravity. In Appendix A, expressions for critical properties of ^{3}He used in the computation are listed. Also, the convection onset near the ^{3}He in the critical region is discussed.

PACS number(s): 44.10.+i, 05.70.Jk, 64.60.−i, 66.10.Cb

I. INTRODUCTION

Recent investigations of pure fluid properties near the liquid-vapor critical point under conditions of reduced gravity field [1–4] have shown that it is very important to assess the equilibrium state of the fluid during the measurements. It is well known that the thermal diffusivity D_T decreases to zero as the critical point (T_c,ρ_c) is approached, where T_c and ρ_c are the critical temperature and mass density [5]. This decrease in D_T produces a "critical slowing down" in the equilibration process when it occurs by diffusion. Several recent results under microgravity conditions show that temperature equilibration at constant average density $\bar{\rho}$ [1] is much faster near the critical point than expected from thermal diffusivity alone, in the absence of convection. This is because of adiabatic energy exchange between the cell boundary and the bulk fluid, as will be discussed in some detail below. By contrast, local density equilibration in the fluid under microgravity conditions is very slow [1,2] near T_c. A complete understanding of the dynamics of temperature, and, especially, density equilibration is therefore necessary for the planning of experiments—both static and dynamic—in space under microgravity conditions.

We have undertaken an experimental program in which ^{3}He fluid density equilibration is investigated following a small step change in temperature of the fluid enclosure. Our experiments were conducted under normal gravity conditions ($g = g_0 = 980$ cm^2/s) in which the average density is kept constant. Surveys include several near-critical isochores and isotherms at temperatures both above T_c (single phase) and below T_c (coexisting liquid and vapor phases). We have used ^{3}He because of the comprehensive survey of the critical properties performed on this fluid in our laboratory [6,7], and because of the practical advantages in carrying out such studies at low temperatures, as will be elaborated in Sec. IV. It needs to be pointed out that the critical behavior of ^{3}He is representative of that of other fluids as well, as can be seen in several reviews [8–10]. In parallel with these experiments, a program of numerical simulation was developed in one dimension (1D). It enabled calculating for $T > T_c$ the response of the local density, pressure, and temperature—as a function both of vertical position z in the cell and of time—following a small step change in temperature of the fluid enclosure. This first paper reports the results of both theory and experiments in the one-phase region above T_c. We plan to present the results of measurements in the two-phase regime for $T < T_c$ in another paper [11]. Preliminary reports on data and numerical computations have been presented elsewhere [12–15].

In this paper, we present the method of numerical simulation in Sec. II with the results and discussion in Sec. III. In Sec. IV we describe the experimental cell, the cryostat, the data acquisition, and reduction routine. The experimental results in connection with the predictions from the numerical simulations are presented and discussed in Sec. V. Finally Sec. VI deals with the summary and outlook for experiments under reduced gravity. Appendix A presents a compendium of parameters used in the numerical calculations and equilibrium

stratification for ^{3}He. Furthermore the onset of convection in the critical region is discussed.

II. NUMERICAL CALCULATION

In this section we start by writing down several equations relevant to the problem of equilibration. We briefly review expressions derived by Onuki and Ferrell [16] that give certain time and space scales that are important in this problem. Also discussed in Ref. [16] is the gravity effect. An outline of the computational procedure is then presented.

An earlier numerical computation was performed for Xe under zero gravity [17]. It was mostly for the temperature equilibration and within short times compared to the system's diffusion time. The computation has recently been extended to density and temperature equilibration under normal gravity [18] over a much wider time range. The authors have treated in detail the spatial and time profiles of pressure, temperature, and density for a temperature quench from 20 to 10 mK above $T_c=289.7$ K for a sample at $\bar{\rho}=\rho_c$. Their computation procedure and grid selection are different from ours, and will be discussed in conjunction with our own numerical results. Also some of their findings differ qualitatively from ours. Because of overlap in some of the respective observations and conclusions, our presentation can be shortened, with due references to [18] at appropriate places.

Xe and ^{3}He are differently affected by gravity, and a measure of their susceptibility is given by the inverse of a characteristic height h_c. Of all fluids, ^{3}He is the most susceptible to gravity while Xe is average, with $h_c^{-1}=3.48\times10^{-3}$ and 1.86×10^{-3} m^{-1}, respectively (See Table 4.2.5 of [9]). Hence we expect that comparable effects of gravity on stratification and on equilibration dynamics should occur at higher reduced temperatures $\epsilon\equiv(T-T_c)/T_c$ for ^{3}He than for Xe.

A. Governing equations

We consider a fluid sealed in a flat, cylindrical, and horizontal cell with height h and diameter d, shown schematically in Fig. 1. In this paper, we treat our problem in one dimension. The predictions thus made are appropriate for the case of $h \ll d$ in which the side wall effect can be neglected. Even though the condition of $h \ll d$ is not met in the real experiment, the predictions from 1D solutions are very helpful in understanding the dynamics that controls equilibration. The thermal diffusivity of the cell wall is much larger than that of ^{3}He, and thus it is treated to be infinite; as a result, the temperature gradients in the fluid enclosure can be neglected without affecting the study of the temperature equilibration in the fluid. The system is initially in equilibrium at T_0. The problem consists then in calculating the density, temperature, and pressure profiles $\rho(z,t)$, $T(z,t)$, and $P(z,t)$ following a temperature change ΔT of the cell wall as shown in Fig. 1.

Our numerical computations are based on the thermodynamic expressions presented in [16] where the flow velocity was neglected. The one-dimensional differential

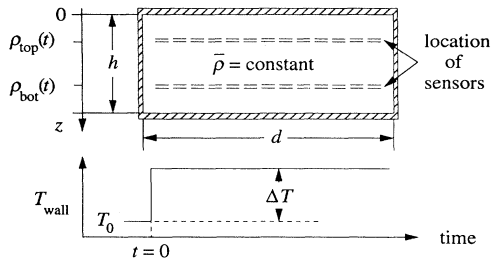

FIG. 1. Top: Schematic view of the flat cell for fluid density measurement at constant average density. Bottom: Temperature step ΔT of the cell versus time t.

equation for entropy transport is given by

$$\rho T\frac{\partial s}{\partial t}=\frac{\partial}{\partial z}\lambda\frac{\partial T}{\partial z} . \tag{1}$$

Here λ is the thermal conductivity and s the entropy per unit mass. When temperature T and pressure P are chosen to be independent thermodynamic variables, Eq. (1) becomes

$$\frac{\partial T}{\partial t}-\left[1-\frac{1}{\gamma}\right]\left[\frac{\partial T}{\partial P}\right]_\rho\frac{\partial P}{\partial t}=\frac{1}{\rho c_P}\frac{\partial}{\partial z}\lambda\frac{\partial T}{\partial z} , \tag{2}$$

where $\gamma\equiv c_P/c_V$ is the ratio of specific heat at constant pressure over specific heat at constant volume. When flow velocity is neglected, the Navier-Stokes equation reduces to

$$\frac{\partial P(z,t)}{\partial z}=g\rho(z,t) . \tag{3}$$

This approximation assumes that the heat conducting fluid in consideration is under hydrodynamic equilibrium at any time. It is valid throughout the fluid layer especially in the late stage when equilibration becomes progressively diffusive. Recently, Boukari, Pego, and Gammon [18] have treated the problem more completely and have shown that the contribution of flow velocity was small enough to be negligible. Furthermore, the change in density is linked to the changes in pressure and temperature linearly through the differential equation of state:

$$\frac{\partial\rho}{\partial t}=\left[\frac{\partial\rho}{\partial T}\right]_P\frac{\partial T}{\partial t}+\left[\frac{\partial\rho}{\partial P}\right]_T\frac{\partial P}{\partial t} . \tag{4}$$

Equations (2) and (3) are solved numerically with the measured static and transport properties of ^{3}He [6,7]. The details of the computation are given in Secs. II C and II D.

B. The Onuki-Ferrell approximations

In Ref. 16, Onuki and Ferrell gave a description for the temperature and density changes inside a fluid layer following a small temperature step $\Delta T \ll (T-T_c)$ of the fluid enclosure, as shown in Fig. 1. As the temperature of the boundary fluid layer rises with that of the solid wall, the fluid within it expands. The expansion produces a

sound wave that propagates back and forth through the layer and causes a fast adiabatic energy transfer to the interior of the fluid. This process is similar to a piston compressing and expanding on a working fluid. The temperature of the bulk fluid then rises very fast through this "piston effect" to *nearly* the wall temperature in a very short time. The lower limit of the expected time scale for this process is the acoustic time defined as $t_{ac}=h/c$ where c is the fluid sound velocity. For a fluid sufficiently close to the critical point where $\gamma \gg 1$ and under zero gravity, the adiabatic energy transfer takes place over a time of the order of

$$t_1=\frac{h^2}{4\gamma^2 D_T} . \tag{5}$$

Here $D_T=\lambda/\rho c_P$ is the thermal diffusivity. As we shall see from numerical calculations, the interior temperature change δT of the fluid reaches about 70% of its final value ΔT by t_1. For $0<t<\gamma^2 t_1=h^2/4D_T$ the width w of the thermal boundary layer increases diffusively as [19]

$$w=\left[\frac{4}{\pi}D_T t\right]^{1/2} . \tag{6}$$

There is a broad intermediate time range $t_1<t<\gamma^2 t_1$ over which one finds $[1-\langle \delta T\rangle(t)/\Delta T]\propto t^{-1/2}$. Here $\langle \delta T\rangle(t)$ is the spatial average of the deviation $\delta T(z,t)$ from the initial equilibrium value. At times $t>\gamma^2 t_1$, an exponential decay of the temperature transient is predicted and the relaxation time is then given by

$$\tau=\frac{h^2}{4\pi^2 D_T} . \tag{7}$$

This time constant is shorter by a factor of 4 than if equilibrium was reached under conditions of constant pressure instead of constant average density. Since D_T goes to zero as T_c is approached, the vanishing of the spatial temperature inhomogeneity $\delta T-\langle \delta T\rangle$ will undergo critical slowing down.

As for the density equilibration in the same situation of zero gravity, Onuki and Ferrell [16] demonstrate that

$$\delta\rho=\left[\frac{\partial\rho}{\partial T}\right]_P[\delta T-\langle \delta T\rangle] . \tag{8}$$

Equation (8) implies that, even though the diffusive tail of the temperature inhomogeneity is difficult to observe due to finite instrumental resolution, information on it can be gained from the measurement of the density transient. Here the spatial temperature inhomogeneity is considerably amplified through multiplication with the thermal expansion coefficient $(\partial\rho/\partial T)_P$ that diverges as T_c is approached. For ^{3}He the magnitude of the dimensionless multiplication factor $(\partial\rho/\partial T)_P(T_c/\rho_c)$ is of the order of 10^5 at $\epsilon=1\times10^{-5}$. It is thus clear that a measurable slow density equilibration results from the diffusive tail of the temperature equilibration.

Onuki and Ferrell [16] have also discussed the effect of gravity on the characteristic time t_1 of the adiabatic energy transfer. For the fluid with $\bar{\rho}=\rho_c$, most of the fluid is off the critical isochore under the influence of gravity when the temperature is close to T_c. The characteristic time t_1 then becomes

$$t_g\sim\frac{h^2}{4(D_T)_b}\left[\frac{\langle C_V\rangle}{(C_P)_b}\right]^2 , \tag{9}$$

where $\langle C_V\rangle$ is the spatial average of C_V over the whole fluid layer and $(D_T)_b$ and $(C_P)_b$ are the properties at the fluid boundaries prior to the temperature change. The calculated t_g and t_{ac} for ^{3}He are presented in Fig. 2. Here the cell height is chosen to be $h=0.43$ cm which corresponds to our experimental system and the sound velocity c is calculated at critical isochore in the limit of zero frequency [20]. We find that t_g levels off due to density stratification for $\epsilon<10^{-3}$. Hence the temperature equilibration achieved by the piston effect takes a longer time under the earth's gravity than under zero gravity. On the other hand, t_g is much longer than t_{ac} in the experimentally accessible temperature range. This means that the piston effect will not be hindered by the sound wave propagation under the earth's gravity in contrast to the case of zero gravity.

The characteristic times discussed above are appropriate for the ideal situation of infinite thermal diffusivity of the cell walls. A theory taking into account the enclosure's finite thermal diffusivity is described in [21]. In our experiment, a temperature step takes approximately 1–2 s due to the thermal inertia of the apparatus and the time constant of the electronics (see Sec. IV B). The fluid equilibration at times of less than 3 s is therefore governed by this time, which is much longer than the time scale of the piston effect, even in the gravity field near T_c.

C. Computational procedure

The pressure P in the fluid comes from three contributions as discussed by Onuki and Ferrell [16],

$$P(z,t)=P_{eq}(z)+\delta P_0(t)+\delta P_1(z,t) . \tag{10}$$

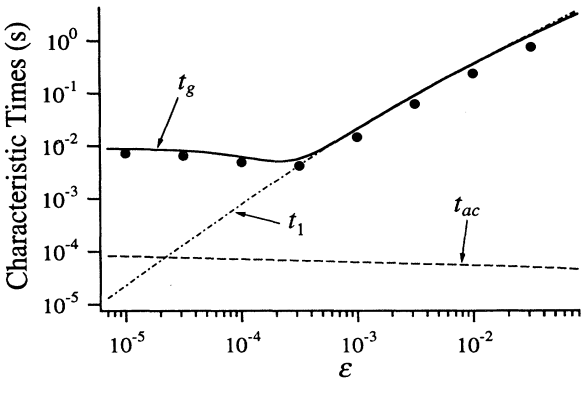

FIG. 2. Characteristic times t_{ac}, t_1, and t_g as defined in the text and in Eqs. (5) and (9), plotted versus ϵ along the critical isochore. The solid circles mark the time when the maximum of the rms density inhomogeneity is predicted from computer simulations (Sec. III).

Here $P_{eq}(z)$ is the equilibrium pressure before the temperature step, $\delta P_0(t)$ is the homogeneous pressure change after the step and $\delta P_1(z,t)$ is induced by the local density variation $\delta\rho(z,t)$. By spatially integrating Eq. (3), we have

$$P(z=h,t)-P(z=0,t)=g\int_0^h \rho(z,t)dz=\bar{\rho}gh \ . \tag{11}$$

Based on Eqs. (10) and (11) one has at the boundaries $\delta P_1(0,t)=\delta P_1(h,t)=0$ due to the mass conservation. Our computation takes advantage of the resulting periodic boundary condition for δP. Taking now a partial time derivative on Eqs. (3) and (11), and using Eq. (4), we have

$$\frac{\partial Y}{\partial z}=g\left[\left[\frac{\partial\rho}{\partial T}\right]_P\frac{\partial T}{\partial t}+\left[\frac{\partial\rho}{\partial P}\right]_T Y\right], \qquad Y(z=0)=Y(z=h) \ , \tag{12}$$

where

$$Y(z,t)\equiv\frac{\partial P(z,t)}{\partial t} \ ,$$

$$\frac{\partial T}{\partial t}-\left[1-\frac{1}{\gamma}\right]\left[\frac{\partial T}{\partial P}\right]_\rho Y=\frac{1}{\rho c_P}\frac{\partial}{\partial z}\lambda\frac{\partial T}{\partial z} \ , \tag{13}$$

$$T(z,t=0)=T_i, \quad T(z=0,t)=T(z=h,t)=T_f \ .$$

In solving Eqs. (12) and (13) numerically, Y is always taken at the $(n+1)$th time step; a smooth transition from the Crank-Nicholson scheme to the fully implicit method [22] is used for T depending on the differencing time step Δt. Although the restriction for a stable solution on the maximum Δt is removed, the existence of strong nonlinearity forces us to try various sizes of Δt to obtain convergent and accurate solution. Once a 1D grid is set, T_i and Y_i are sandwiched to form a $2N$ vector; the coefficients from the finite difference of Eqs. (12) and (13) form a band diagonal matrix. The simultaneous solutions of T and Y at the $(n+1)$th time are obtained by solving the matrix through LU decomposition and backsubstitution [22]. These intermediate T_i's and Y_i's are used to calculate $\delta\rho_i$'s from Eq. (4). Then the intermediate T_i's and ρ_i's are used to update the spatially varying thermodynamic coefficients. Usually up to three such iterations are needed to achieve a convergence for each time step.

Near the critical temperature T_c, several thermodynamic properties, such as C_P and λ, are strongly divergent as T_c is approached along the critical isochore. Then Eqs. (12) and (13) become highly nonlinear. The nonlinear coupling between temperature and density is included through the iteration as mentioned above. In Appendix A we indicate the relevant equations for the measured static and dynamic properties that were fitted to scaling expressions. In Appendix B we describe the grid generation used in the computation.

III. COMPUTATION RESULTS

Only the fluid with $\bar{\rho}=\rho_c$ and cell height $h=0.43$ cm is considered in this section. To visualize what is happening within the fluid layer after a step change in temperature of the horizontal boundaries, we will show (a) diagrams of the spatial distribution of temperature, pressure, and density at given times and (b) temporal profiles of these quantities at specific locations, especially at the locations of the density sensors in our experimental cell which are separated from the top and bottom boundaries by $0.267h$.

The following notation of scaled variables will be used:

Reduced temperature: $\epsilon\equiv\dfrac{T-T_c}{T_c}$,

temperature step: $\Delta\epsilon\equiv\dfrac{\Delta T}{T_c}$,

density deviation from ρ_c: $\Delta\rho\equiv\dfrac{(\rho-\rho_c)}{\rho_c}$,

density change from initial equilibrium: $\delta\rho\equiv\delta(\Delta\rho)$,
rms density change from initial equilibrium:

$$\delta\rho_{\rm rms}\equiv\langle\delta\rho^2\rangle^{1/2} \ ,$$

where $\langle\ \rangle$ is the spatial average. After the step $\Delta\epsilon$, the local changes in the fluid are denoted by $\delta\epsilon(z,t)$, $\delta\rho(z,t)$, and $\delta P_1(z,t)$ while $\delta\rho_{\rm rms}$ characterizes the overall density change. All the quantities are scaled by their critical parameters $T_c=3.310$ K, $\rho_c=0.0414$ g/cm^3, and $P_c=1.146\times10^6$ dyn/cm^2.

It is instructive to first describe the dynamics of equilibration when the isothermal compressibility β_T is very small, so that the density stratification changes are negligible for a step $\Delta\epsilon$ in the earth's gravity field. Following this, the diagrams are shown for moderate and strong stratification.

A. Small stratification

Figure 3 shows a spatial profile for $\epsilon=3\times10^{-2}$ and a step $\Delta\epsilon=1.5\times10^{-3}$. The three superposed graphs show the changes $\delta\epsilon(z,t)$, $\delta P_1(z,t)$, and $\delta\rho(z,t)$ at four time instants. The initial conditions for the computer simulation are shown by the dotted lines at $t=0^+$.

By $t=t_1=1.22$ s, the pressure δP_0 caused by the piston effect has risen very rapidly to 0.003. The work done by this pressure change has raised the temperature uniformly in the bulk fluid to $\delta\epsilon/\Delta\epsilon=0.56$ while diffusion from the wall produces boundary layers of effective width $w/h=0.0071$. The temperature step increase at the wall has caused a sharp density decrease within the thin boundary layer because of the fluid's large thermal expansion coefficient. The fluid expansion within the boundary layer is compensated by the density increase in the interior of the fluid for total mass conserved. Hence the direct consequence of the piston effect is the density disturbance in the entire fluid layer from its initial equilibrium. The density change results in the pressure change $\delta P_1(z,t)$ through the coupling of gravity, whose magnitude is much smaller than that of $\delta P_0(t)$. As time increases beyond t_1, the boundary layer continues to widen; the local density in the bulk fluid reaches a z-dependent peak in such a way as to cancel out in an integral fashion the den-

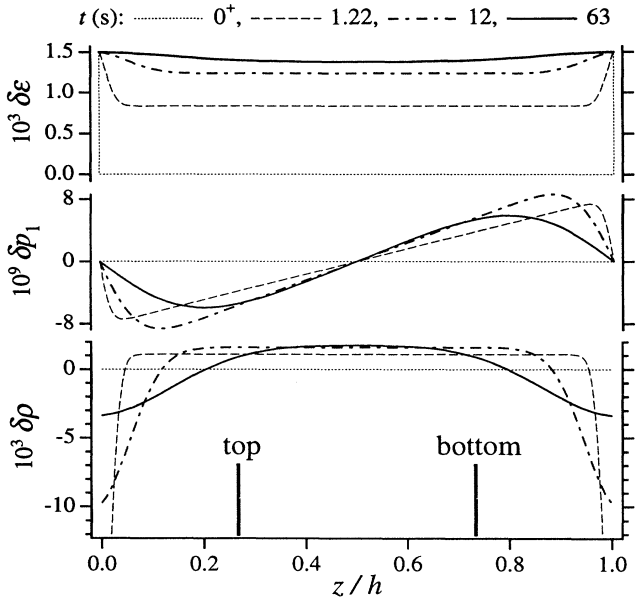

FIG. 3. Simulated spatial profiles for $\delta\epsilon$, δP_1, and $\delta\rho$ versus z at three instants after the temperature step $\Delta\epsilon=1.5\times10^{-3}$ at $\epsilon=3\times10^{-2}$.

sity decrease in the expanding boundary layer. Due to the boundary layer expansion, the fluid within approximately $h/4$ from the walls will approach final equilibrium from the opposite direction from that of the fluid in the middle.

In Fig. 4, we present the temporal profiles of the average temperature change $\langle\delta\epsilon\rangle$, the temperature inhomogeneity $[\delta\epsilon-\langle\delta\epsilon\rangle]$, the density induced pressure change δP_1, and $\delta\rho$ at the locations of both density sensors and in the cell middle. It can be clearly seen that $\delta\rho$ is simply a mirror reflection of $[\delta\epsilon-\langle\delta\epsilon\rangle]$, in agreement with Eq. (8). The density equilibration appears to depends strongly on position, being slowest in the middle.

In Fig. 5, the relaxation of $\delta\rho$ is shown on a semilogarithmic scale that emphasizes the behavior at long times. The asymptotic behavior at all three positions can be approximated by a single exponential function

$$\delta\rho(z,t)=\delta\rho(z,\infty)+A(z)\exp(-t/\tau)\ . \tag{14}$$

The resulting relaxation time τ agrees with the prediction by Eq. (7) as shown in Table I. Because the density deviation in the interior of the fluid results from the boundary expansion whereas the boundary layer itself expands diffusively, $\delta\rho$ reaches an asymptotic regime earlier at the locations closer to the boundaries. By the time the asymptotic regime is reached at the location of the density sensors, $\delta\rho$ has already decayed to a magnitude less than 10^{-5}. One can therefore expect that this asymptotic regime will be observable over a restricted range of time when the limited instrumental resolution, $\delta\rho=2\times10^{-6}$, is considered (see Sec. IV). In a typical experiment, the observed decay will be approximated by Eq. (14). Such a derived effective relaxation time might not necessarily be the asymptotic one, as will be discussed in detail in Sec. IV.

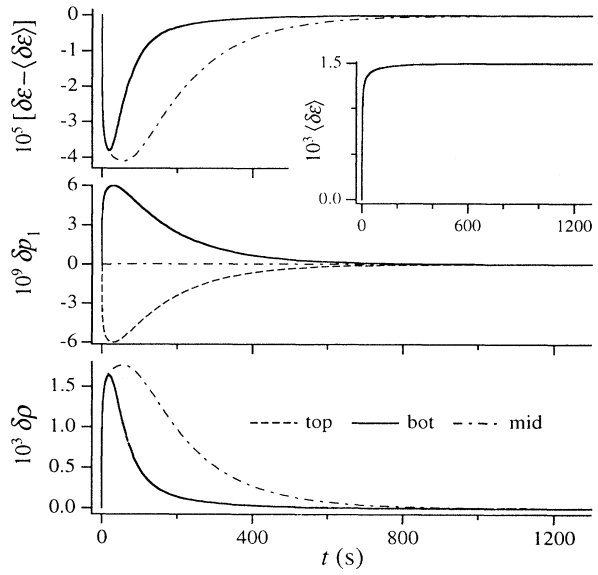

FIG. 4. Temporal profile for the average temperature $\langle\delta\epsilon\rangle$, the temperature inhomogeneity $[\delta\epsilon-\langle\delta\epsilon\rangle]$, δP_1, and $\delta\rho$ taken at the two sensor locations and the middle of the fluid layer, following the temperature step $\Delta\epsilon=1.5\times10^{-3}$ at $\epsilon=3\times10^{-2}$. In the top and bottom graphs, the solid and dashed curves overlap.

Also shown in Fig. 5 is the density change $\delta\rho_{\rm rms}$. Because the contributions from regions close to the boundaries are included in this average, $\delta\rho_{\rm rms}$ reaches an asymptotic exponential decay mode much sooner than the density deviations at the sensor locations. The $\delta\rho_{\rm rms}$ peak appears at $t\sim t_g$.

B. Moderate stratification

In the presence of observable stratification, one can approximately picture the total density change $\delta\rho(z,t)$ as a sum of two contributions:

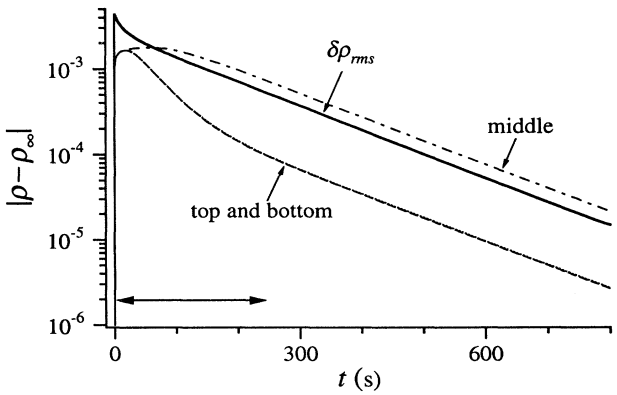

FIG. 5. Semilogarithmic plot of $|\delta\rho(t)-\delta\rho(\infty)|$ taken at the two sensor locations (top and bottom) and the fluid middle for $\Delta\epsilon=1.5\times10^{-3}$ at $\epsilon=3\times10^{-2}$. $\delta\rho_{\rm rms}$ indicates the overall density deviation from initial equilibrium. The double-arrowed line marks the limit of experimental resolution in $\delta\rho$.

TABLE I. The *asymptotic* relaxation times τ for ^{3}He in flat cell with $h=0.43$ cm, as a function of ϵ, with $\bar{\rho}=\rho_c$, under normal gravity. Column 2 is from the simulated density decay; columns 3 and 4 show the approximations with two types of spatial average on D_T as described in text; column 5 is for $D_T(\rho_c)$—this would correspond to the situation of zero gravity.

ϵ	$\tau(g_0)$ (s)	τ_a (s)	τ_b (s)	$\tau(\rho_c)$ (s)
8×10^{-2}	6.6×10^{1}	6.61×10^{1}	6.61×10^{1}	6.61×10^{1}
3×10^{-2}	1.61×10^{2}	1.61×10^{2}	1.61×10^{2}	1.61×10^{2}
1×10^{-2}	4.66×10^{2}	4.67×10^{2}	4.67×10^{2}	4.67×10^{2}
3×10^{-3}	1.47×10^{3}	1.46×10^{3}	1.46×10^{3}	1.45×10^{3}
1×10^{-3}	3.76×10^{3}	3.77×10^{3}	3.78×10^{3}	3.75×10^{3}
3×10^{-4}	8.88×10^{3}	8.96×10^{3}	9.00×10^{3}	9.32×10^{3}
1×10^{-4}	$\sim1.23\times10^{4}$	1.15×10^{4}	1.27×10^{4}	2.03×10^{4}
3×10^{-5}	1.31×10^{4}	1.02×10^{4}	1.29×10^{4}	3.22×10^{4}
1×10^{-5}	1.47×10^{4}	9.53×10^{3}	1.23×10^{4}	8.96×10^{4}
5×10^{-6}	1.52×10^{4}	9.35×10^{3}	1.20×10^{4}	1.37×10^{5}
1×10^{-6}	1.53×10^{4}	9.19×10^{3}	1.17×10^{4}	3.64×10^{5}

$$\delta\rho(z,t)=\delta\rho_{\rm PT}(z,t)+\delta\rho_{\rm grav}(z,t)\ . \tag{15}$$

Here $\delta\rho_{\rm PT}$ indicates density disturbance caused by the piston effect as we have discussed in the previous subsection; and $\delta\rho_{\rm grav}$ is the result from the stratification change upon a temperature step $\Delta\epsilon$. In the case of $\Delta\epsilon>0$, the stratification will decrease due to the decreasing compressibility. Consequently, the density in the bottom (top) half of the cell will decrease (increase) as the fluid of $\bar{\rho}=\rho_c$ progresses towards a new equilibrium, leading to $\delta\rho_{\rm grav}$ asymmetric about the cell middle. On the other hand, as we have seen in the previous subsection, $\delta\rho_{\rm PT}$ is symmetric about the cell middle, and it decays back to zero as time tends to infinity after having been raised through a maximum by the piston effect. Hence we expect that the two density sensors (located as shown in Fig. 1) will record a substantially different time profile. The density transient at $z=h/2$ will only be affected by the piston effect. Shown in Fig. 6 are the average temperature change and temperature inhomogeneity, δP_1, and $\delta\rho$ as functions of time; they are presented in the same format as in Fig. 4 to emphasize the differences with the situation in the absence of stratification. After reaching the peaks of density deviation, $\delta\rho_{\rm PT}$ and $\delta\rho_{\rm grav}$ always relax in the same direction at the bottom sensor location but into opposite direction at the top sensor location. The competition between $\delta\rho_{\rm PT}$ and $\delta\rho_{\rm grav}$ at the top sensor location gives the false impression that the density transients at the top and bottom sensor location decay with different time constants; in some situations this competition prevents the use of a simple exponential function to approximate the density transient decay. This can be seen in a more expanded presentation of the absolute values $|\delta\rho(t)-\delta\rho(\infty)|$ versus time on a semilogarithmic scale in Fig. 7. In fact, $\delta\rho_{\rm top}(t)$ decreases beyond its equilibrium values before it is corrected back towards it, causing a sharp dip in the plot at $t=4\times10^3$ s. A fit of Eq. (14) to the three individual curves for $t>2\times10^4$ s gives the same asymptotic relaxation time τ within the error of determination, in good agreement with the predicted value (see Table I). Clearly stratification has not affected τ. However, for this value of $\Delta\epsilon$, the *asymptotic* behavior is not observable for $\delta\rho_{\rm top}$, because of the limit imposed by the instrumental resolution, as shown by the double-arrowed line in Fig. 7. This demonstrates that the "effective" relaxation times $\tau_{\rm eff}$ obtained by fitting Eq. (14) to the experimental data might give different results for the bottom and top sensors. This is a general observation at all temperatures we have already mentioned previously [14].

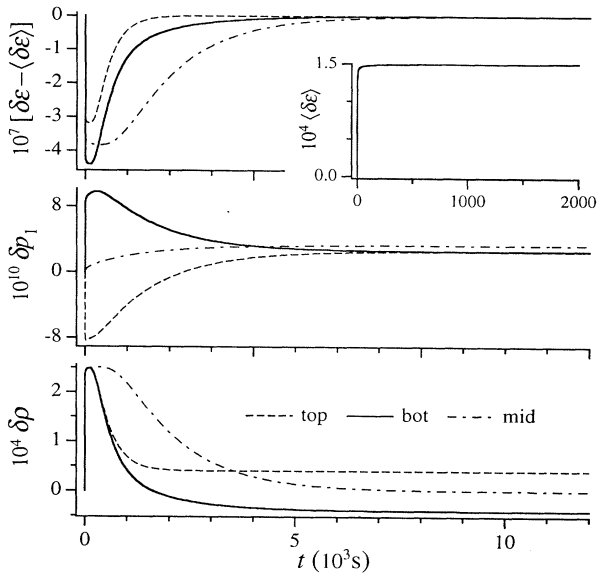

FIG. 6. Temporal profile for the average temperature $\langle\delta\epsilon\rangle$, the temperature inhomogeneity $[\delta\epsilon-\langle\delta\epsilon\rangle]$, δP_1, and $\delta\rho$ taken at the two sensor locations and the middle of the fluid layer, following the temperature step $\Delta\epsilon=1.5\times10^{-4}$ at $\epsilon=3\times10^{-3}$.

In the presence of even modest density stratification, the temperature equilibration is affected in a very sensitive way. As we compare $[\delta\epsilon-\langle\delta\epsilon\rangle]$ in Figs. 4 and 6, the temperature at the top sensor location equilibrates

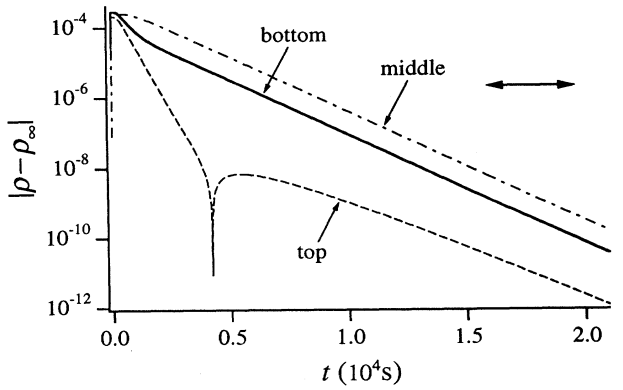

FIG. 7. Semilogarithmic plot of $|\delta\rho(t)-\delta\rho(\infty)|$ taken at the two sensor locations (top and bottom) and the fluid middle for $\Delta\epsilon=1.5\times10^{-4}$ at $\epsilon=3\times10^{-3}$. The double-arrowed line marks the limit of experimental resolution in $\delta\rho$.

ahead of the one at the bottom. This can be explained by reexamining Eq. (2). The coupling between the pressure and temperature is through $(\partial T/\partial P)_\rho$ which varies slightly with density as shown in Fig. 21(b) below. Therefore even a homogeneous pressure change δP_0 caused by the piston effect converts its mechanical energy into internal energy in an inhomogeneous way, resulting in a spatial temperature gradient in the bulk fluid immediately after a temperature change at the boundary.

C. Strong stratification

As the critical temperature is approached, the roles played by $\delta\rho_{\rm PT}$ and $\delta\rho_{\rm grav}$ are changed in favor of the latter. The trend can be best illustrated in Fig. 8, where we plot the respective amplitudes of $\delta\rho_{\rm PT}$ and $\delta\rho_{\rm grav}$ for a small temperature step as a function of ϵ. The dashed line is taken from the maximum value of $(\delta\rho_{\rm PT})_{\rm rms}$ as shown in Fig. 5 divided by $\Delta\epsilon$. It gives an idea of how strong a spatial inhomogeneity in density can be induced by the piston effect. The solid line is the rms average of $\delta\rho$ at $t=\infty$ divided by $\Delta\epsilon$. It indicates the amount of the change in $\delta\rho$ due to the change in stratification for the same temperature change. As we expected, $\delta\rho_{\rm grav}$ dominates at small ϵ while $\delta\rho_{\rm PT}$ does at large ϵ. In between, there is a crossover region where the observable density profiles $\rho(\text{top},t)$ will be complex.

In Fig. 9 we show for $\epsilon=3\times10^{-4}$ and $\Delta\epsilon=1.5\times10^{-5}$ the time profiles of $[\delta\epsilon-\langle\delta\epsilon\rangle]$, $\delta P_1(z,t)$, and $\delta\rho(z,t)$ at the three locations as described before. At $\epsilon=3\times10^{-4}$, the piston effect still rapidly equilibrates the average temperature at the fluid interior, in the same way as in Figs. 3 and 6. Its effect on density deviation is still visible in the plot. However, the density changes due to stratification after a long time are much larger than the ones by the piston effect at these particular positions in space. A semilogarithmic plot in Fig. 10 for the top and bottom sensors confirms the density transient decays to be exponential for $t>1\times10^4$ s. A fit to the straight portions of the curves gives again the same value of τ for each of them, which is compared with the result from Eq. (7) where D_T has been taken on the critical isochore (see Table I). Only a slight effect on τ from stratification is noticed, which is consistent with arguments presented by Berg [23], who developed expressions for the asymptotic behavior of density transients in the presence of gravity.

It should be pointed out that the temporal profiles of the spatial inhomogeneity in temperature and pressure have dramatically changed compared to the corresponding ones with moderate stratification in Fig. 6. As in the case of moderate stratification, the work done by the homogeneous δP_0 on the bulk fluid is converted inhomogeneously into internal energy. As a result, the temperature at the top half cell equilibrates not only ahead of the

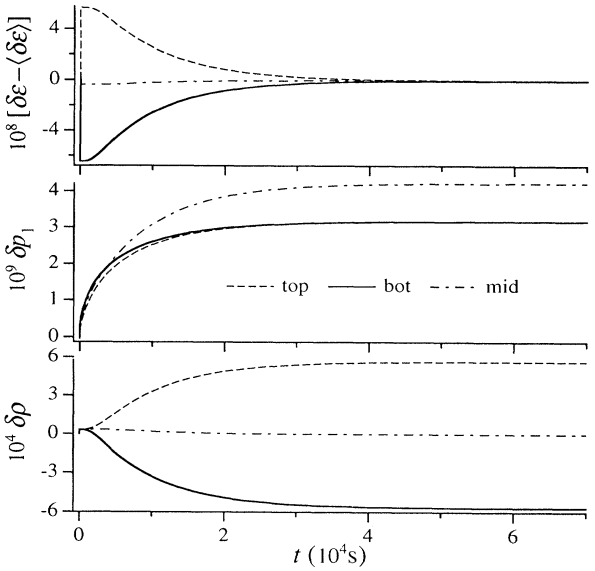

FIG. 9. Temporal profile for the average temperatures $\langle\delta\epsilon\rangle$, the temperature inhomogeneity $[\delta\epsilon-\langle\delta\epsilon\rangle]$, δP_1, and $\delta\rho$ taken at the two sensor locations and the middle of the fluid layer, following the temperature step $\Delta\epsilon=1.5\times10^{-5}$ at $\epsilon=3\times10^{-4}$.

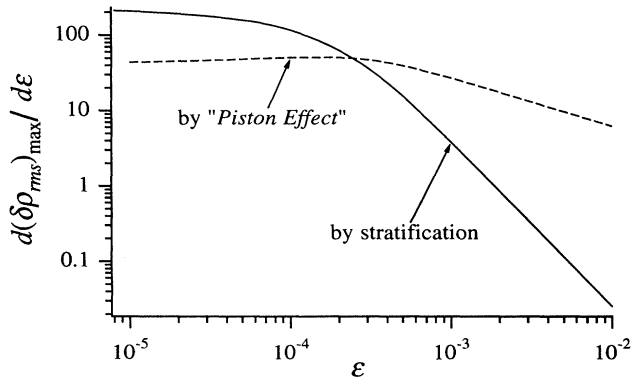

FIG. 8. Sensitivity of $\delta\rho_{\rm PT}$ and $\delta\rho_{\rm grav}$ to a small temperature step $\Delta\epsilon$ as a function of ϵ. Here $d(\delta\rho_{\rm PT})/d\epsilon$ is calculated from the maximum value of $(\delta\rho_{\rm PT})_{\rm rms}$ as shown in Fig. 5, and $d(\delta\rho_{\rm grav})/d\epsilon$ is from the rms average of $\delta\rho$ at $t=\infty$. Both the calculations are made with $h=0.43$ cm, $g=g_0$, and $\Delta\epsilon=1\times10^{-3}\epsilon$.

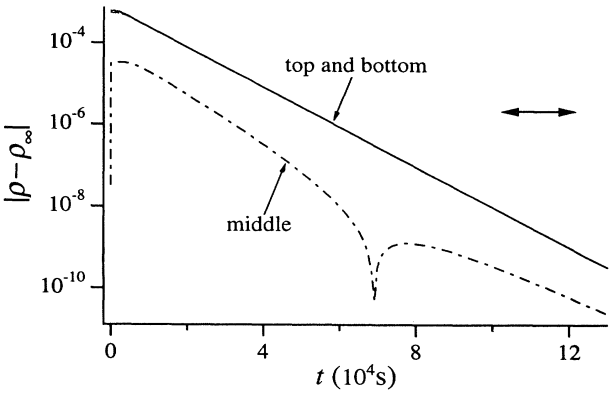

FIG. 10. Semilogarithmic plot of $|\delta\rho(t)-\delta\rho(\infty)|$ taken at the two sensor locations (top and bottom) and the fluid middle for $\Delta\epsilon=1.5\times10^{-5}$ at $\epsilon=3\times10^{-4}$.

one at the bottom half (Fig. 6) but also ahead of the average temperature (Fig. 9). This leads to the surprising phenomenon that the temperature starts to overshoot its equilibration value $\Delta\epsilon$ near the top boundary, as the piston effect continues to draw energy from the bottom boundary layer and equilibrates the temperature in the whole bulk fluid. This phenomenon has been independently found and discussed by Boukari, Pego, and Gammon [18]. The spatial distribution of the overshooting and its evolution are presented in Fig. 11 for $\epsilon=3\times10^{-4}$ and a step $\Delta\epsilon=1.5\times10^{-5}$, where $\delta\epsilon(z,t)$, $\delta P_1(z,t)$, and $\delta\rho(z,t)$ are plotted against z at several instants. The details will be discussed in Appendix C. Due to the temperature overshoot, the density transient at $z=h/2$, induced initially by the piston effect, goes beyond its new equilibrium value. The density transient shows a sharp dip in Fig. 10 for $\delta\rho_{\rm mid}$ at $t\approx7\times10^4$ s ($\approx7.5\tau$). For $t>10\tau=1.2\times10^5$ s, its decay becomes parallel with the ones at other locations. Clearly the overshooting will have a strong effect on the determination of effective relaxation time at $z=h/2$.

D. The density relaxation times at normal gravity

Because of the complex behavior of the density transient decay, it is important to describe clearly the method of determining the effective relaxation time $\tau_{\rm eff}$ in a consistent way. Hence the temperature steps $\Delta\epsilon$ used in the simulation are comparable with the ones taken in the experiment described in Sec. V. After the transient has decayed to roughly $\frac{1}{4}$ of its maximum amplitude, we fit Eq. (14) to the remaining portion. In the worst case, such as when the piston effect dominates the transients, the $\tau_{\rm eff}$ determined from the same fit, but over about $\frac{1}{3}$ of the remaining decay, can have a value that is 15% smaller than the previous one. Furthermore, if a Gaussian noise with the amplitude of 2×10^{-6} and rms of 0.5 is added to the simulated transient before the fit, the deduced $\tau_{\rm eff}$ will be lowered by up to 25%. This noise level corresponds to that in the density measurements, described in Sec. V. Given this value, the larger the $\Delta\epsilon$, the larger the portion of the transient closer to the asymptotic regime that will be resolvable, which results in larger value of $\tau_{\rm eff}$ (see Fig. 5).

From Fig. 7 it can be seen that the determination of $\tau_{\rm eff}$ will then depend on the spatial location. In Fig. 12 we present the $\tau_{\rm eff}$ at both sensor locations obtained from the fit without adding the Gaussian noise. For $\epsilon<1\times10^{-3}$, the fit is determined by the stratification alone. The jump in the value of $\tau_{\rm eff}$ (top) in the region of $\epsilon\approx1\times10^{-3}$ is due to the competition between the relaxations of the piston effect and of the stratification. For $\epsilon>1\times10^{-3}$, the result from the fit reflects mostly the relaxation of the piston effect.

The interesting question raised from the numerical simulation is whether there is an asymptotic relaxation time which is independent of spatial location in the presence of strong stratification. In the case of small stratification, the whole system equilibrates with a single asymptotic relaxation time for $t>2\tau$ (Fig. 5). For $\epsilon<1\times10^{-3}$, the temperature overshoot and its subsequent decay complicate the density equilibration. For $2\times10^{-4}<\epsilon<1\times10^{-3}$, where stratification is approximately linear in the vertical position z, the overshooting effect is small, and the long term density transients ($2\tau<t<30\tau$) have a single relaxation time at all the locations except near the cell's middle. For $\epsilon\le5\times10^{-5}$, where stratification is strongly nonlinear, our computations show that the overshooting effects have disappeared for $t>1.5\times10^5$ s, and then the whole system equilibrates

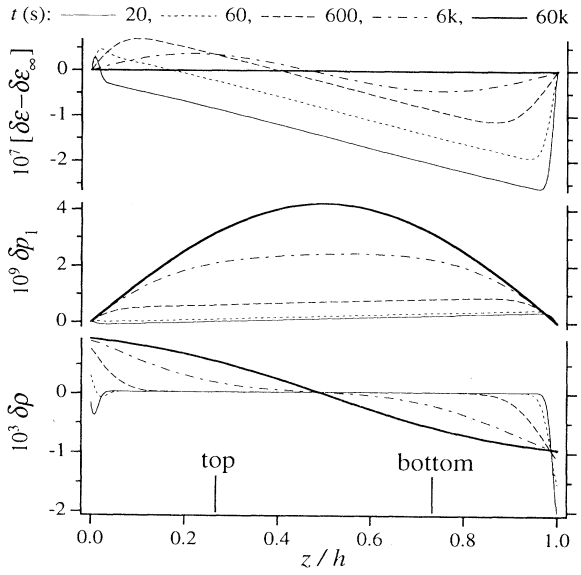

FIG. 11. Simulated spatial profiles for $\delta\epsilon$, δP_1, and $\delta\rho$ versus z at five instants after the temperature step $\Delta\epsilon=1.5\times10^{-5}$ at $\epsilon=3\times10^{-4}$.

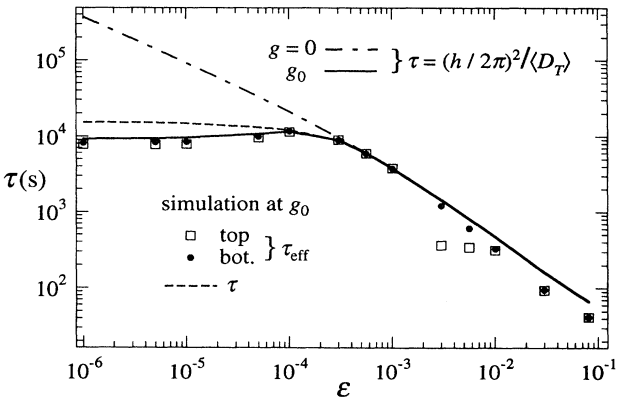

FIG. 12. Computed relaxation times for top and bottom density sensors as a function of ϵ. The symbols are for $\tau_{\rm eff}$, as described in the text. The dashed line is obtained from the simulated transients in the asymptotic regime (column 2 of Table I). The solid line is the approximation of the asymptotic τ calculated from Eq. (7) with spatially averaged $\langle D_T\rangle$ to account for stratification. The dot-dashed line is from Eq. (7) with D_T taken at ρ_c, which corresponds to zero gravity. For $\epsilon>3\times10^{-4}$ the three curves overlap.

with a single relaxation time. In the crossover region, overshooting effects are predicted for $t > 20\tau$. We did not continue to search for the unique relaxation time after $t > 30\tau$. The dashed line in Fig. 12 shows the asymptotic relaxation time τ as obtained from the fit to the straight portion of the density transient decays at locations other than $z = h/2$ (see Fig. 10). The values are also presented in column 2 of Table I. The data obtained within the crossover region are only approximate.

At present, we do not have a clear understanding of the dynamics of the temperature overshooting (see Appendix C). We hope that some of the observations from our numerical simulations will stimulate further theoretical study of this problem. In the absence of a rigorous proof, we assume that the asymptotic relaxation regime exists even in the presence of strong stratification. If as a first approximation we are to take stratification into account in the calculation of τ via Eq. (7), we can try spatial averages $\langle D_T^{-1} \rangle$ and $\langle D_T \rangle^{-1}$ in the place of D_T^{-1} in Eq. (7). The result of these averages is shown in columns 3 and 4 of Table I by $\tau_a(g_0)$ and $\tau_b(g_0)$. The calculations using $\langle D_T \rangle^{-1}$ give the solid line in Fig. 12, but we specify that this is only an approximation.

All the time constants τ_{eff}, τ, τ_a, and τ_b show an initial divergence for $\epsilon > 3\times10^{-4}$, and they gradually level off into a horizontal plateau. This is caused by the gravity field since near T_c all the fluid sample, except for a very thin layer in the middle, is off the critical isochore.

The investigation for Xe in Ref. [18] was performed with $h = 5$ mm and a temperature quench ($\Delta\epsilon < 0$) from $\epsilon_i = 6.9\times10^{-5}$ to $\epsilon_f = 3.5\times10^{-5}$. In Figs. 6 and 7 of [18], the authors indicate that for Xe the asymptotic exponential decays have not been reached for times up to 27 h, and the effective exponent for their decay was found to vary randomly with z.

We point out that for Xe the temperature range used in [18] is located right at the crossover between linear and nonlinear stratification. The observations by Boukari, Pego, and Gammon then agree in general with what we have discussed above. We have indeed seen in the corresponding range for ^{3}He that the effects of the temperature overshoot prevent us from determining an asymptotic relaxation time up to $t \sim 30\tau$. Also, as we can see from Fig. 11, δP_1 still changes substantially for $t > 0.64\tau$; some nondiffusive temperature change will result from the adiabatical work of this spatially varying parameter. It would be interesting to have density transient decays generated for Xe at longer times and other values of ϵ to see whether asymptotic exponential decays are predicted with a τ independent of z.

E. Equilibration under reduced gravitational acceleration

Under reduced gravity, taken arbitrarily as $g = g_0\times10^{-3}$, the equilibration dynamics is substantially changed, since now stratification is much smaller. Our numerical simulation then shows that for $\epsilon > 10^{-5}$ the density transients $\delta\rho(z,t)$ have the same shape as those in Fig. 4, namely, there is a substantial spike due to the piston effect immediately following the temperature step, and a subsequent decay. The divergence of the relaxation time as T_c is approached is strong at least down to $\epsilon = 10^{-6}$. With the reduced stratification, the phenomenon of temperature overshooting the equilibrium value over a certain range of z occurs at lower values of ϵ; hence the transient decays become exponential at earlier times than under normal gravity.

F. Temperature ramping at zero gravity

In Sec. II B, it was shown that the piston effect equilibrates the temperature in the bulk fluid in a very short time, but it disturbs the density from its equilibrium distribution. This phenomenon exists with or without gravity. The resulting density disturbance follows the temperature inhomogeneity as predicted by Eq. (8). The overall density deviation, characterized with $\delta\rho_{\text{rms}}$, reaches a peak at a time approximately equal to t_g (Fig. 2) with an amplitude proportional to ΔT (Fig. 8). It then decays diffusively with a very long time constant, as shown in Fig. 5.

Our calculation under zero gravity endeavors to answer the following questions. (1) Will the $\delta\rho_{\text{rms}}$, caused by the piston effect, keep growing as the temperature of a fluid enclosure continues to change? (2) At what temperature ramping rate can a measurement of a fluid property be considered as in a quasiequilibrium state? The calculation was carried out for ^{3}He with $\bar{\rho} = \rho_c$ and $h = 0.43$ cm. It covers the reduced temperature range of $1\times10^{-5} \le \epsilon_{\text{wall}} \le 8\times10^{-2}$ for two ramping rates $|d\epsilon/dt| = 3.0\times10^{-4}$/h and 3.0×10^{-5}/h. In both warming and cooling directions, the ramping started with an equilibrium state. Our calculations show that spatial inhomogeneity in ϵ is always less than 4×10^{-7} for the ramping rate of 3.0×10^{-4}/h. Figure 13 shows the computed $\delta\rho_{\text{rms}}$ versus the reduced temperature of the enclosure, ϵ_{wall}, on a logarithmic plot for cooling and warming.

When the cooling starts, there is an immediate buildup of $\delta\rho_{\text{rms}}$ through the piston effect. The sharp departure from the vertical rise indicates that the system reaches a quasisteady state at $t \approx 5\tau$. As ϵ_{wall} decreases, the thermal expansion coefficient becomes larger, resulting in a larger density inhomogeneity off the critical isochore, which in

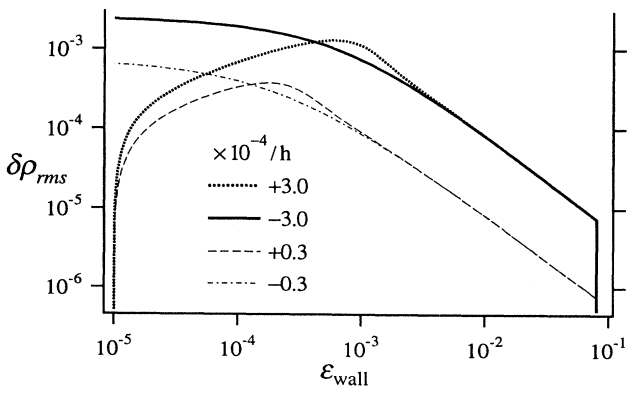

FIG. 13. Logarithmic plot of $\delta\rho_{\text{rms}}$ vs the reduced temperature at the cell wall, ϵ_{wall}, for four constant ramping rates $d\epsilon_{\text{wall}}/dt$. The ramping starts at equilibrium for both directions.

turn increases the overall thermal diffusion rate and reduces the temperature inhomogeneity. This interplay causes $\delta\rho_{\rm rms}$ to level off to the values of 2.3×10^{-3} and 6.4×10^{-4} for the two ramping rates at $\epsilon_{\rm wall}=1\times10^{-5}$.

Upon warming, the initial rapid $\delta\rho_{\rm rms}$ increase is the result from increasing temperature inhomogeneity. Then the increasing diffusion rate "catches up" with the given ramping rate, leading to a maximum value in $\delta\rho_{\rm rms}$. After that, $\delta\rho_{\rm rms}$ decreases with increasing $\epsilon_{\rm wall}$ until the sharp change at $\epsilon=8\times10^{-2}$. (We note that the starting temperature was above T_c. Had it been below T_c—as during typical calorimetric experiments [24] — the $\delta\rho_{\rm rms}$ could be expected to be much larger because of the coexisting two phases. Such a ramping calculation remains to be carried out.)

The two ramping rates chosen in our calculation are comparable with $|d\epsilon/dt|=1.2\times10^{-3}$/h and 1.9×10^{-4}/h, used by Straub and Haupt in recent calorimetric experiments with the fluid SF_6 under microgravity conditions [26]. The effect on the calorimetric measurements caused by $\delta\rho_{\rm rms}$ can now be assessed. Using the computed spatial distributions of temperature and density when $\epsilon_{\rm wall}$ is ramped from 1×10^{-2} to 1×10^{-5}, we calculated that $1-\langle C_V\rangle/C_V(\rho_c)\leq3\times10^{-3}$ and 2.5×10^{-4} for the cooling rates of 3.0×10^{-4}/h and 3.0×10^{-5}/h, respectively.

In their experiments, Straub and Haupt started from a reduced temperature $\epsilon=10^{-3}$ and cooled toward $\epsilon=0$. They reported observing the C_V singularity in agreement with predictions. Their ramping rate mentioned above is thus slow enough to avoid the effects from an excessive $\delta\rho_{\rm rms}$, and this is consistent with the result of our calculations.

G. Summary of the numerical simulations

Detailed numerical simulations of the equilibration process for ^{3}He fluid have been made along its critical isochore over the reduced temperature range $5\times10^{-6}<\epsilon<8\times10^{-2}$. The evolution of thermodynamic variables (temperature, pressure, and density) was followed both spatially and temporally under conditions of normal and reduced gravitational acceleration g. The density is a good property for studying the equilibration through the slow diffusive process that dominates at long times. When stratification is small, the equilibration process leads to an exponentially decaying transient with an asymptotic relaxation time τ. However, the asymptotic regime may not be accessible in an experiment due to finite instrumental resolution; an effective time $\tau_{\rm eff}$, with $\tau_{\rm eff}<\tau$, is more likely to be deduced from available transients when an exponential function "appears" to be a good approximation.

When stratification becomes significant, the spatial and temporal evolution of the thermodynamic variables becomes more complex because of competition between the processes of the diffusion and adiabatic energy transfer into internal energy. As a result, at certain values of z and t the variables will overshoot their final equilibrium value to which they then slowly relax back. Simulations then show that the overshooting can prevent the transients from entering the asymptotic regime even for $t>20\tau$ when $\epsilon\sim1\times10^{-4}$. For $\epsilon<1\times10^{-4}$, the overshooting takes place at earlier times and the whole system eventually equilibrates with an asymptotic relaxation time τ.

Under normal gravity, $g=g_0$, the crossover from linear to nonlinear stratification starts at $\epsilon\approx3\times10^{-4}$ for ^{3}He with $h=0.43$ cm. This crossover corresponds to the reduced temperature where the simulated $\tau_{\rm eff}$ values start to level off after diverging with decreasing ϵ. Under reduced gravity the crossover temperature is pushed towards lower values.

It is interesting to compare the evolution of the thermodynamic variables in the situation we have discussed with that in a thermal conductivity cell [28]. Here the fluid is again contained between two parallel and horizontal plates, but the temperature of the bottom plate, $T(z=h)$, is kept constant. A heat current is switched on at time 0^+, and crosses the fluid layer in a downward direction. One observes the temperature difference $\Delta T=T(z=0,t)-T(z=h)$. The general equations described in Sec. III B are the same, but the boundary conditions are different. In the case of the thermal conductivity experiment, the temperature increase at the top boundary causes the fluid to expand within the top boundary layer and the resulting piston effect increases the temperature in the bulk fluid just as we have seen in Fig. 3. However, this increased bulk temperature drops sharply across the bottom diffusive layer to the constant bottom boundary temperature, resulting in a compressed fluid within the layer. As a result, the piston effects at the two boundaries nearly cancel each other. Furthermore, the measured ΔT is roughly the sum of the temperature differences established *diffusively* within the two boundary layers. Hence ΔT across the fluid layer does not exhibit any sudden change in its time evolution. Numerical simulations, carried out by us but not reported here, show that $\delta T(z=0)$ enters the asymptotic regime earlier than the local thermodynamic variables in the bulk fluid and can be observed experimentally. The measured relaxation time is smaller by a factor of 4 compared with equilibration under constant pressure [28]. The good agreement between the measured relaxation times [6] and their analysis in [28] is *quantitative* confirmation of the inclusion of the adiabatic energy transfer term in the entropy transport equation when the fluid system is held at constant volume.

IV. APPARATUS AND EXPERIMENTAL PROCEDURES

A. General remarks

Our method to detect density changes with high resolution uses the measurements of the dielectric constant ϵ^* from two thin horizontal capacitors, located in the upper and in the lower half of a flat copper cell (see Fig. 14). The density is then obtained via the Clausius-Mossotti relation. All the measurements of density and temperature

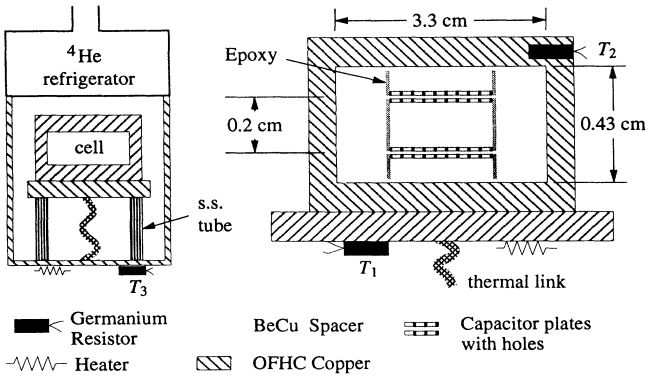

FIG. 14. Schematic presentation of the vacuum-insulated density cell assembly (left) and of the flat cell with superposed density sensors (right).

are made with ac bridge circuits. Such a circuit consists [29] of a ratio transformer, a reference element mounted on a temperature-regulated platform to insure long term temperature stability, and a phase-sensitive detector with its output recorded by a computer.

B. The density cell

The flat horizontal cell, made of oxygen-free high-conductivity (OFHC) copper is shown schematically in Fig. 14. It was constructed for density stratification measurements near the critical point of ^{3}He [7] and the tricritical point of ^{3}He-^{4}He mixtures [30]. For convenience we repeat briefly the cell specifications and describe the temperature control.

Two pairs of thin perforated stainless steel blades with 28% transparency form the capacitors that are separated by 2.0 mm, while the total fluid layer height in the cell is 4.3 mm and the layer diameter is 33 mm. The capacitors, each sampling over a height of 0.1 mm, are symmetrically placed about the cell's midplane, as shown in Fig. 14. Beryllium-copper spacers with holes of 2 and 5 mm form a rigid support and an electrical shielding for the capacitor assembly. These holes enable rapid vertical fluid flow. The two capacitors measure the local density $\rho_{\rm top}$ and $\rho_{\rm bot}$ at the top and bottom positions $z_{\rm top}$ and $z_{\rm bot}$. They are connected individually to an ac bridge circuit. With a driving voltage of 11 V at a frequency of 1.2 kHz, a density resolution and stability of 2 parts in 10^6 over a period of several hours is achieved.

C. Temperature control

The cell is bolted to a temperature-regulated platform with a heater and a germanium thermometer T_1 on it. This thermometer and a reference wire-wound resistor are part of a second ac bridge circuit with its offset feeding back into the heater. Thus the temperature T_1 can be regulated to 3 μK. The cell temperature is further monitored by a second thermometer T_2 inserted into the cell wall at the top (see Fig. 14).

A second platform is kept at a temperature T_3 between $T=2.8$ and 3.2 K. It is regulated within 20 mK with an analog temperature controller. This platform supports the cell platform with three stainless-steel tubes of low thermal conductivity. The controlled temperature difference between the two platforms produces a heat current through the thermal coupling of a braid of copper wires.

The temperature T_1 of the cell platform is controlled digitally by a computer. When the offset in the feedback loop is changed, the heat current through the thermal coupling adjusts itself, causing a rapid temperature change of the cell platform. Nonlinear algorithms are used in the digital control in order to avoid significant temperature overshooting and oscillations after the step, so that the initial response of the local density can be compared with predictions. The regulation of better than 3 μK is reached within 3 s after a step change, and is shown by the monitoring temperature T_2.

The presence and importance of the convection effects could be assessed by taking both positive and negative temperature steps, as will be discussed in Sec. IV.

D. Calibration procedures and data acquisition

Following initial thermometer calibration, the critical point had to be located.

It is known from the scaling properties of fluids nearly their critical point [9] that $(\partial\rho/\partial\mu)_T$ is a symmetric function of $|\Delta\rho|$ which permits an accurate location of ρ_c. Above T_c, we measured along several isotherms the difference $(\rho_{\rm bot}-\rho_{\rm top})$, which is proportional to $(\partial\rho/\partial\mu)_T$ with a maximum at ρ_c. From the location of this maximum, the critical density was then determined within 0.2%.

Below T_c, the coexistence curve was measured at several temperatures. By using the known equation of the coexistence curve and also of the compressibility along the critical isochore, as compared with our data, T_c could be located within 20 μK.

For a sequence of equilibration measurements, both positive and negative ΔT steps were taken once equilibration from the previous step had been reached. The numerical analysis of the recorded curves $\rho_{\rm bot}(t)$ and $\rho_{\rm top}(t)$ from the bottom and top sensor was obtained by fitting them to a single [Eq. (14)] or double exponential decay of the form.

$$\delta\rho(t)=\delta\rho(\infty)+A_{\rm eff}\exp(-t/\tau_{\rm eff})+A_1\exp(-t/\tau_1)\ , \tag{16}$$

where $\tau_{\rm eff}>\tau_1$. This fit is limited to a time range where the signal-to-noise ratio is acceptable, namely, where $|\delta\rho(t)|$ is larger than 2×10^{-6}. As shown in Sec. III E, $\tau_{\rm eff}$ is usually smaller than the asymptotic τ.

V. RESULTS AND DISCUSSION

We first present experimental results of the density transient $\delta\rho(t)$ at $\bar{\rho}=\rho_c$ after a ΔT perturbation, and compare them with numerical simulations for the same

temperature step. We choose three representative reduced temperatures: (a) $\epsilon=1\times10^{-2}$ at which stratification is negligible, (b) $\epsilon=1\times10^{-3}$, in a regime where stratification becomes significant, and (c) $\epsilon=3\times10^{-5}$ where stratification is very important. Following this, we present equilibration data along two isotherms for the first two regimes and finally we show a comparison of the effective relaxation times from experiments and predictions.

A. Negligible stratification

In Fig. 15 we show the density transients for both sensors in a standard sequence of temperature steps $|\Delta\epsilon|=2.5\times10^{-5}$ at $\epsilon=1\times10^{-2}$. The top trace shows the time dependence of T_2 which is sharp with negligible overshoot at each step. The lower two traces represent $\rho_{top}(t)$ and $\rho_{bot}(t)$. Immediately after the step, whether positive or negative, the density shows a sharp spike where $d\rho/d\epsilon>0$. This is consistent with the theoretical description of the piston effect: the sudden wall temperature increase (decrease) leads to a fast thermal expansion (contraction) in a boundary layer. Because of mass conservation in the cell, the density measured away from the boundary layer will respond by increasing (decreasing). At this temperature, the compressibility β_T and its response to temperature change are small. Because of the negligible change in stratification the density, disturbed by the piston effect, will relax via a diffusive process back to its initial value. This can be seen from the traces of $\rho(t)$ at two equilibrium states before and after the temperature step: there is no visible density shift. To compare the experimentally observed equilibration process with the numerical simulation, we transfer one portion of $\rho_{bot}(t)$ from Fig. 15 for examination into Fig. 16. The simulated curve is computed without any adjustable parameters for the same spatial location z and temperature step as in the experiment. Several remarks need to be made:

First, the observed noise in the transients determines the instrumental resolution in density, which we estimate to be 2×10^{-6}. The fit of Eq. (14) to the observed experimental decay that follows the spike yields the observable and effective relaxation time τ_{eff}. As we have discussed before, such a τ_{eff} usually is smaller than the τ that is obtained in the asymptotic regime.

Second, we note that while the *magnitude* and the general shape of the computed density change are in good agreement with the experimental observations, the simulated transient has a much wider spike and its decay takes a longer time than does the observed. From Eq. (4) in [19] and Eq. (3) in [25], we see that the temperature equilibration by the piston effect depends on an experimental ratio, S/V, where S is the boundary area for net heat flux and V is the fluid volume. The larger the S/V ratio, the larger the adiabatic energy generated at the boundaries for a finite amount of fluid, and the faster the temperature will be equilibrated. In our experiment, (a) heat also flows in through the side wall of the cell; (b) the sensor supports reduce the effective volume for the fluid. The larger value of S/V in the experiment compared to the one in the 1D model might possibly explain the difference in time scales of the two curves in Fig. 16. However, this difference in the S/V ratio does not affect the spike magnitudes of the density transients since the total density change from the boundary layers will remain the same.

Third, in this temperature range, where stratification is negligible, the time evolution of the density is calculated to be nearly symmetric about the cell midpoint for $t<\tau$, namely, $\rho(z,t)=\rho(h-z,t)$. However, the experimental data in Fig. 15 show some differences between the top and bottom sensors. These differences in the transient shapes yield slightly different effective relaxation times. We suspect that the differences might be caused by our cell departing from a simple 1D geometry, and the complication introduced by the sensor supports. We do not believe that convection causes the differences since the absolute magnitude of the change stays nearly the same

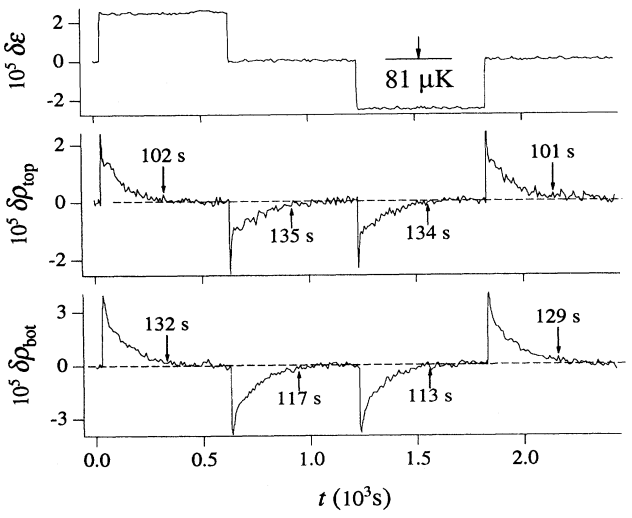

FIG. 15. Representative sequence of temperature changes and the measured temporal density profiles. The first trace is the temperature change at the cell's wall followed by those of the density changes $\delta\rho$ as recorded by the two sensors. The measurement was taken at $\epsilon=1\times10^{-2}$ with $\Delta\epsilon=2.5\times10^{-5}$.

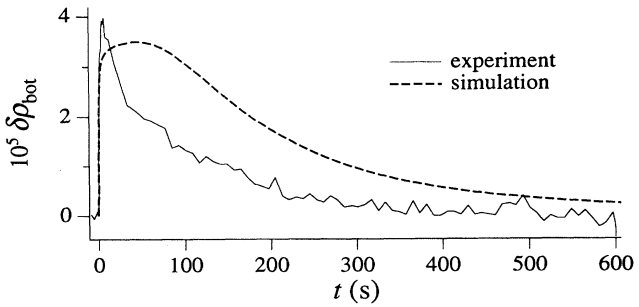

FIG. 16. Comparison between calculation and experiment of density transients at the bottom sensor at $\epsilon=1\times10^{-2}$ with $\Delta\epsilon=2.5\times10^{-5}$.

upon warming and cooling steps for either the top or bottom, and furthermore the convection would have decayed before the long term transient could be affected. We calculated the onset of convection for our cell dimension to be about $\Delta\epsilon=2.2\times10^{-6}$ (see Appendix D for convection onset calculations), which is smaller than the $\Delta\epsilon=2.5\times10^{-5}$ used in our sequence. However, the piston effect is expected to suppress the onset of convection by quickly reducing the temperature difference between the interior and boundaries within a few seconds. The same argument applies to experiments closer to T_c.

B. Moderate stratification

In Fig. 17 we show the density transients observed for $\epsilon=1\times10^{-3}$ and $\Delta\epsilon=\pm1.2\times10^{-5}$ during a similar sequence of temperature steps (the complete sequence is shown in [13]). We note the difference, both in the shape and in the time scale, from those in Fig. 15. The shape of $\rho(z,t)$ at the sensor location has been explained in Sec. IV with a simple model when stratification changes can be detected. The good agreement for the shape and amplitude proves that the equilibration process is qualitatively understood, and that again there is little evidence for convection. However, the predicted time scale (simulated $\tau_{\rm eff}$) is longer than the observed one by a factor of 6.

C. Strong stratification

In this regime, the density difference between the top and the bottom of the fluid layer is of the order of several percent of ρ_c (see Appendix A for the stratification profiles). In Fig. 18(a), we show the absolute value of the density transients observed for $\epsilon=3\times10^{-5}$ and after a temperature step $\Delta\epsilon=-3\times10^{-6}$. The amplitude of the bottom transient $\rho(t=0)-\rho(\infty)$ is normalized to the top one for the purpose of comparing with the computer simulation. Because of the long relaxation times and slow drift in temperature control, fluctuations in the amplitudes of $\rho(t=0)-\rho(\infty)$ will be enhanced close to T_c. However, the amplitude difference between the top and bottom transients was found to be random, and on average they individually are consistent with the simulation. This justifies the normalization. We note that the magnitude of the fast initial density change from the piston effect has become small in comparison with the large change from the stratification for both sensors. The top sensor seems to have recorded an effectively faster transient than the bottom one.

The simulated density transients for the same temperature change and sensor locations are shown in Fig. 18(b). The time scales of the experimental and simulated evolutions are now different by a factor of ≈10, as we can tell from the respective values of $\tau_{\rm eff}$. The $\tau_{\rm eff}$ obtained experimentally is smaller at the top sensor than at the bottom one. The difference is in the same direction for the $\tau_{\rm eff}$ obtained from the computer simulation, where the difference, however, is hardly visible.

In Fig. 18(c), we show on a semilogarithmic plot the simulated transient $|\rho(t)-\rho(\infty)|$ versus time at four locations including both top and bottom sensors for the same change of $\Delta\epsilon$. The density overshoot is clearly seen as a dip at $z=0.1h$ and the top sensor location. Due to the overshoot, the $\tau_{\rm eff}$ will be smaller at the top two locations

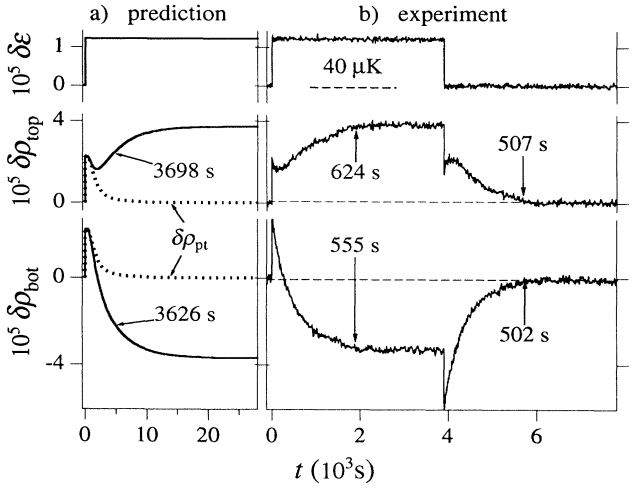

FIG. 17. Comparison between calculation (left) and experiment (right), for the density change recorded by top and bottom sensors at $\epsilon=1\times10^{-3}$ for a step $\Delta\epsilon=1.2\times10^{-5}$. The dotted line on the left is $\delta\rho_{\rm PT}$, computed without gravity. The numbers tagged on the curves are $\tau_{\rm eff}$. Note the difference in the time scale presentation between the left and right, chosen so as to enable comparison of the profile shapes.

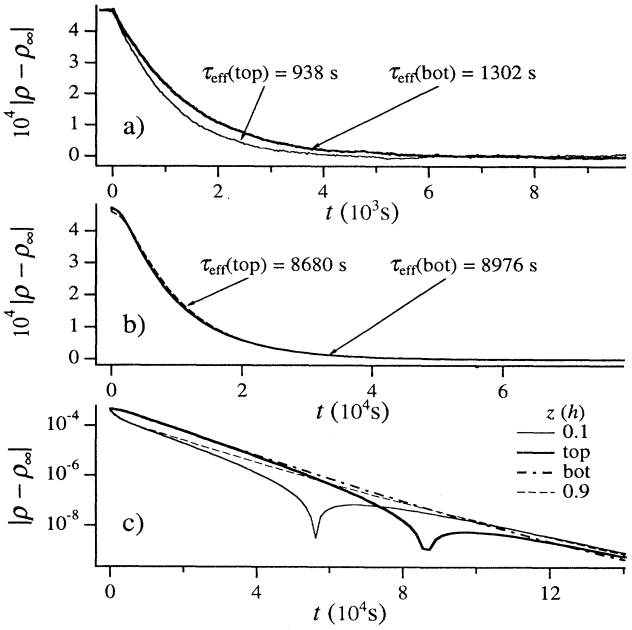

FIG. 18. Absolute density changes at the top and bottom sensors for $\epsilon=3\times10^{-5}$ and $\Delta\epsilon=-3\times10^{-6}$, as described in the text. (a) Experiment. (b) Simulation. (c) Simulation on semilogarithmic plot at four spatial locations. The damped density oscillation around its value ρ_∞ (shown as sharp dips) is suspected to be the possible origin for the difference in the $\tau_{\rm eff}$ between the top and bottom sensors.

compared to the two below $z=h/2$. The difference in τ_{eff} gets larger closer to the boundary. We suspect that the overshoot could be the origin for the smaller observed τ_{eff} at the top sensor compared to the value at the bottom sensor even though the time scale of the computed transient is larger by a factor of 10 than the experimental one. The asymptotic regime is only reached at a time well beyond that of the overshoot and is not accessible to experimental observation. The difference between the simulated τ_{eff} and τ will be shown in the next section.

D. The effective relaxation times

We have seen in the previous three subsections that as ϵ decreases the time scales increase and so does the difference between the experimentally observed and the simulated transient times τ_{eff} as described in Sec. III D. The overall results are reflected by equilibration time constants versus ϵ as shown in Fig. 19. Here Eqs. (14) and (16) are used to fit the experimental transients for obtaining τ_{eff}. (Due to the small values of $\Delta\epsilon$ used in the experiment for $\epsilon > 1\times10^{-3}$, the amplitude of the measured density deviation was not large compared to the instrumental noise, and more than $\frac{1}{4}$ of the remaining transient tail portion was used in the fit which could lower the value of τ_{eff}.) Although the representation of the experimental $|\rho(t)-\rho(\infty)|$ appears to be a straight line on semilogarithmic plots, we have seen from the numerical simulations that the relaxation times obtained from them may not be the asymptotic ones which are shown in Fig. 12.

Average values of τ_{eff} over successive cooling and warming transients for the data are shown in Fig. 19. It is clear that both the experiment and simulation show that as the critical point is approached the relaxation times first diverge and then level off. However, the divergence of the calculated τ_{eff} is steeper than of the experimental one. The cause of this discrepancy is not understood, but it may have its origin with the beryllium-copper supports of the capacitors that complicate the cell geometry. We estimate the D_T of beryllium-copper to be greater than 10 cm^2/s at $T=3$ K, which is much larger than for ^{3}He.

The leveling off of the relaxation time for $\epsilon < 1\times10^{-4}$ is understood in terms of density stratification, as discussed in Sec. IV B. Also we see from Fig. 18 that the τ_{eff} fitted from the simulated transients is smaller at the top sensor than at the bottom one. One possible explanation is the density overshoot at the top sensor location. We note in Fig. 19 some discontinuity in the experimental τ_{eff}(top) data near $\epsilon=5\times10^{-3}$. This is not experimental scatter, but represents a genuine effect where one passes from the regime where the piston effect dominates to that where stratification dominates in total density change. The effect is also shown in the simulation results. (See the discussion in Sec. IV B.)

In Fig. 20 we compare the experimental and simulated τ_{eff} along the isotherms $\epsilon=1\times10^{-2}$ and $\epsilon=5\times10^{-4}$. The data for $\Delta\rho=0$ are the same as those shown in Fig. 19. Also shown on the same plot is the asymptotic τ. For $\epsilon=1\times10^{-2}$, it is the small stratification that causes the simulated τ_{eff} for the top sensor to be smaller than for the bottom sensor while the difference between the measured τ_{eff} at the two locations is not clear. For $\epsilon=5\times10^{-4}$, the simulated τ_{eff}(top) displays the discontinuity at the same average density as the measured one.

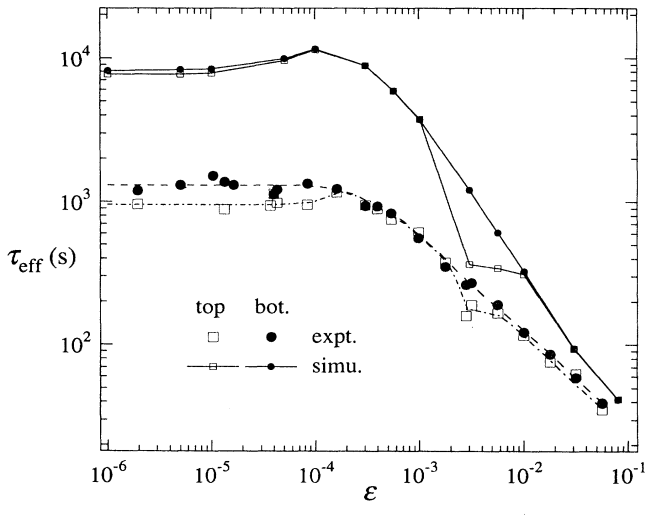

FIG. 19. The effective relaxation times for density equilibration at the top and bottom sensors. The open squares and solid circles are for the experimentally observed τ_{eff} and the dashed and dot-dashed lines are guides to the eye. The same symbols, smaller in size and connected with solid lines, represent the simulated τ_{eff} at the same vertical locations as described in the text.

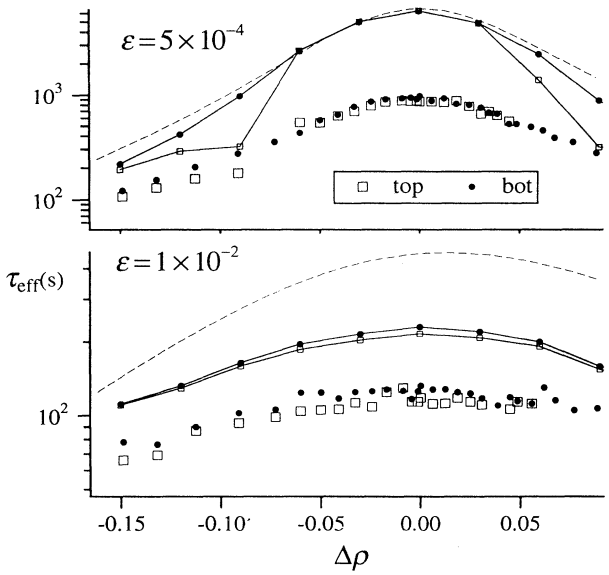

FIG. 20. The relaxation time along two isotherms versus $\Delta\rho$. Symbols are for the experimentally observed relaxation times τ_{eff} at the two sensor locations. The same symbols, smaller in size and connected with solid lines, are for the simulated τ_{eff} at the same vertical locations, as described in the text. Dashed lines represent the asymptotic relaxation times τ calculated from Eq. (7) as described in the text.

This discontinuity is also observed for the critical isochore, as shown in Fig. 19, and is due to the transition from the piston effect dominated regime to the stratification dominated one. The τ_{eff} obtained by the simulation is systematically larger than the one observed in the experiment. This difference, already present along the critical isochore, is maintained along isotherms as well.

VI. SUMMARY

In this paper we have presented a theoretical and an experimental study of the local density change $\delta\rho(z,t)$ inside a pure fluid at constant volume in the region above the critical point. This study was carried out with ^{3}He and the experiment was performed in a flat cylindrical cell with two superposed density sensors, mostly along the critical isochore. Studies were also performed along other near-critical isochores (not presented here) and along isotherms. In this paper we concentrate on the region above T_c, while those below T_c are presented elsewhere [11]. The principal results for the critical isochore are as follows.

(1) At reduced temperatures when stratification through gravitational acceleration is small, both numerical computations and experiments demonstrate a rapid density change throughout the fluid layer (piston effect), immediately following a temperature step. The simulation shows that the shape of $\delta\rho(t)$ is sensitive to the vertical z position, especially when the piston effect dominates and the equilibration process is not yet driven solely by diffusion. Pseudoexponential transient decays are then obtained with effective relaxation times that depend on vertical location. The asymptotic transient decay is always exponential with a relaxation time τ that is the same throughout the fluid, but with amplitudes that are dependent on the vertical position.

(2) There is a good qualitative agreement between the predictions and experiments as far as shape and amplitude of $\delta\rho(t)$ are concerned even though they change considerably over the critical region we have investigated ($10^{-5}<\epsilon<10^{-1}$). However, the peak width of the density change caused by the piston effect is much narrower in the experiment than in the simulation. While there is a fair agreement at $\epsilon=8\times10^{-2}$, the time scale of the numerical calculations becomes systematically larger than that of the experimental equilibration; this discrepancy needs to be understood.

(3) Both simulation and experiment show that the equilibration relaxation time first diverges as T_c is approached and then rolls over to a constant value because of fluid stratification in the cell. The divergence of the predicted relaxation time is stronger than the experimental one and this discrepancy needs to be understood.

(4) The simulation reveals a temperature overshoot starting at the top boundary layer. This overshoot is caused by density stratification and results in complex transients of the density equilibration especially above the middle of the fluid layer. Even though no experiment has reported such an effect directly, the difference between τ_{eff} observed above and below the middle of the fluid layer for $\epsilon<1\times10^{-4}$ can be considered as indirect evidence of the dynamics that causes the overshoot. This assertion is based on the good qualitative agreement of the difference in τ_{eff} obtained between the simulation and experiment.

(5) The simulation also reveals that the stratification only affects the onset of the asymptotic regime around $\epsilon\sim1\times10^{-4}$ where the stratification starts to become nonlinear. Away from this ϵ region, the simulated transients eventually relax asymptotically with a single time constant τ throughout the fluid but with position dependent amplitudes. A further theoretical study is needed to establish rigorously the existence of the asymptotic regime when the strong stratification is present.

The agreement between the simulation and experiment can be expected to become more quantitative when data obtained with a cell having a simpler, more ideal geometry and insulated side walls can be compared with the 1D calculations. Pending these further developments, we can already make predictions of the density perturbation and equilibration after a temperature step under microgravity conditions. There the relaxation times will continue diverging instead of leveling off as T_c is approached.

(6) The overall density inhomogeneity caused by the piston effect will accumulate if the boundary temperature is continuously changed. This accumulation depends on the ramping rate and ramping direction. Our computation gives a useful estimate of how well a property, such as C_V, measured during this ramping can approach its value ideally determined under static conditions.

ACKNOWLEDGMENTS

This research was supported by NASA Grants No. NAGW-3328 and No. NAG5-379. The authors acknowledge conversations with A. Onuki, R. Ferrell, R. F. Berg, J. Straub, L. Eicher, and H. Boukari and correspondence with R. L. Pego.

APPENDIX A: CALCULATIONS OF THERMODYNAMIC PROPERTIES OF ^{3}He

Here we give the expressions that are used to calculate the thermodynamic properties of ^{3}He for any given ϵ and ρ. For the static properties, the calculation is based on the "restricted cubic model" [9]. These expressions are

$$\mu(\rho,T)-\mu(\rho_c,T)=\frac{P_c}{\rho_c}a\theta(1-\theta^2)r^{\beta\delta}\ , \tag{A1a}$$

$$\epsilon\equiv\frac{T-T_c}{T_c}=r(1-b^2\theta^2)\ , \tag{A1b}$$

$$\Delta\rho\equiv\frac{\rho-\rho_c}{\rho_c}=kr^{\beta}\theta(1+c\theta^2)\ . \tag{A1c}$$

In Eq. (A1), r and θ describe the location with respect to the critical point in a parametric space and a and k are fluid dependent parameters, which for ^{3}He are $a=4.09$ and $k=0.819$ (based on a new simultaneous fit to the experimental data of $(\partial P/\partial T)_\rho$ [31] and C_V [32]). We adopt the effective critical exponents as given in Ref. [9].

These are

$$\alpha=0.100,\quad \beta=0.355,\quad \gamma=1.190\ ,$$
$$\nu=0.633,\quad \delta=4.352\ .$$

With the critical exponents listed above, the restricted cubic model yields

$$b^2=\frac{3}{3-2\beta}=1.310,\quad c=\frac{2\beta\delta-3}{3-2\beta}=0.0393\ .$$

Once the critical exponents and the coefficients for the cubic model are selected, the equilibrium density stratification is readily calculated [33].

The dimensionless expressions for the static properties are listed in Table 4.3.3 of Ref. [9]. Here we only present the information on the background contributions for ^{3}He (dimensionless). We assume the pressure coefficient to have an analytic background, i.e.,

$$-\frac{dA_0(\epsilon)}{d\epsilon}=c_0+c_1\epsilon+c_2\epsilon^2$$

with

$$c_0=3.42,\quad c_1=-2.66,\quad c_2=-9.22\ .$$

The regular contribution for specific heat is

$$\left.\frac{C_V}{T}\right|_{\rm reg}=-\frac{d^2A_0(\epsilon)}{d\epsilon^2}-\rho\frac{d^2\mu(\rho_c,\epsilon)}{d\epsilon^2}\ .$$

From Ref. [31], $d^2\mu(\rho_c,\epsilon)/d\epsilon^2$ is independent of ϵ and we have treated $-d^2A_0(\epsilon)/d\epsilon^2$ as a constant. The new fit gives

$$-\frac{d^2A_0(\epsilon)}{d\epsilon^2}=-3.22,\quad \frac{d^2\mu(\rho_c,\epsilon)}{d\epsilon^2}=2.90\ .$$

The thermal conductivity is also assumed to be the sum of a regular and a singular contribution,

$$\lambda=\lambda_{\rm reg}(T,\Delta\rho)+\lambda_{\rm sing}(\epsilon,\Delta\rho)\ . \tag{A2}$$

For $\lambda_{\rm reg}(T,\Delta\rho)$ we ignore the density dependence and use the expression for $\Delta\rho=0$ in [6]. For the singular part, we use the scaling expressions as proposed by Sengers [34],

$$\frac{A\lambda_{\rm sing}}{\Lambda|\Delta\rho|^{-\psi/\beta}}=[f_{k_T}(X)]^{1/2}\ , \tag{A3a}$$

$$f_{k_T}^{-1}(X)=\Gamma\left[h(X)\delta-\frac{X}{\beta}\frac{dh}{dX}\right]\ , \tag{A3b}$$

$$h(X)=E_1\left[1+\frac{X}{X_0}\right]\left[1+E_2\left[1+\frac{X}{X_0}\right]^{2\beta}\right]^{(\gamma-1)/2\beta}\ , \tag{A3c}$$

$$X=\frac{\varepsilon}{|\Delta\rho|^{1/\beta}}\ .$$

For ^{3}He, we have [6]

$$A=1,\quad \Lambda=3.73\times10^{-6}\ \frac{\rm W}{\rm cm\,K},\quad \psi=\gamma/2\ ,$$
$$X_0=0.488,\quad E_1=2.98,\quad E_2=0.281\ .$$

From a combination of the values of ρC_P and λ we obtain the diffusivity D_T. In Fig. 21(a) we present the density stratification of ^{3}He for three values of ϵ, with $\bar\rho=\rho_c$ in the cell of 4.3 cm height and under the earth's gravity. Due to the density stratification, other key thermodynamic properties depend strongly on the vertical position z in the cell as the critical point is approached. For example, in Fig. 21(b), the pressure coefficient $(\partial P/\partial T)_\rho$ varies with z in the same manner as $\Delta\rho$. As a result, even the spatially homogeneous δP_0 produces an inhomogeneous temperature profile. We present in Fig. 21(c) the spatial profile of D_T at the same three isotherms. When strong stratification is present for the fluid of $\bar\rho=\rho_c$, D_T is not symmetric at the top and bottom boundaries. The spatial variation is even sharper for the isothermal compressibility which alters significantly the behavior of ρ near the cell center [Fig. 21(d)]. All these observations point to the necessity of carefully choosing the grid in the computation procedure in order to properly take into account the spatial as well as time variation of thermodynamic parameters.

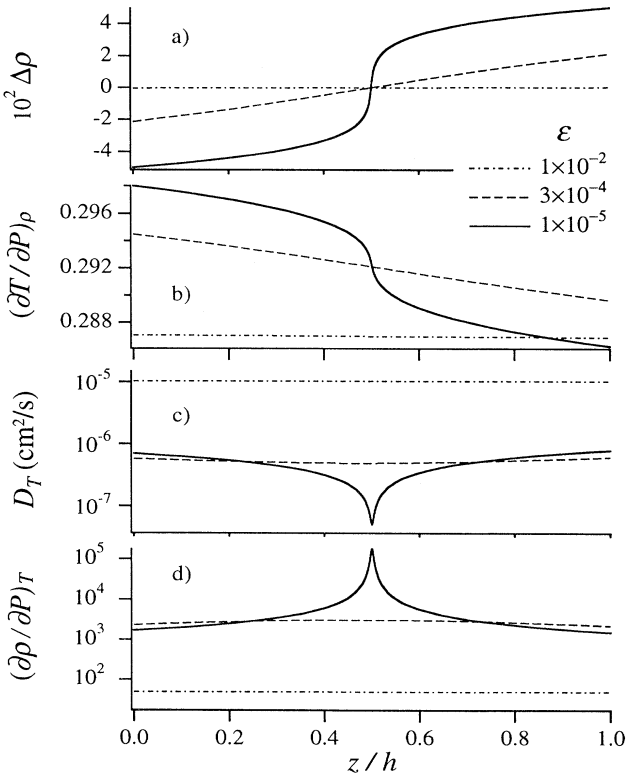

FIG. 21. (a) The equilibrium spatial profiles of ^{3}He density for $g=g_0$ and $h=0.43$ cm at three values of ϵ. (b), (c), and (d) The spatial variations of D_T, $(\partial\rho/\partial P)_T$, and $(\partial P/\partial T)_\rho$ due to the density stratification at the same three values of ϵ. The top of the cell is at $z/h=0$.

APPENDIX B: GRID GENERATION

Once an initial time step Δt_0 is chosen, the boundary layer thickness w is calculated from Eq. (6). A large temperature gradient is expected within the layer at short times. Hence we want a small grid spacing near each of the two cell boundaries. Furthermore, the expected large spatial variations in thermodynamic coefficients within the layer around $\rho=\rho_c$ (see Appendix A) will affect the dynamics in the neighborhood of this layer. In the case of $\bar{\rho}=\rho_c$, this layer is at the midpoint of the fluid sample. Hence a small grid spacing at the cell center is desired. In the rest of this section, the space variable z is scaled with cell height h. We now follow the method described in [35]. The grid spacings at cell boundary and at the cell center are chosen as

$$\Delta z_0=\frac{w}{M}, \quad \Delta z_{N/2}=\frac{\Delta z_0}{A^2},$$

where M is the number of points inside the boundary layer, and N is the total number of grid points which we set to be odd. We then set up a grid point distribution based on

$$\begin{aligned} z_i &= \frac{0.5u(i)}{A+(1-A)u(i)}, \quad 0\le i\le N/2, \\ z_i &= 1-x_{N-1-i}, \quad N/2<i<N, \end{aligned} \tag{B1}$$

where

$$u(i)=\frac{1}{2}\left\{1-\frac{\tanh[\sigma(1-4i/N)]}{\tanh(\sigma)}\right\} \tag{B2}$$

is the conventional stretching function [35]. The damping factor σ is obtained by solving the relation

$$\sinh(2\sigma)-\frac{2\sigma}{NA\Delta z_0}=0. \tag{B3}$$

As time evolves, the large initial temperature gradients within the calculation domain relax. Hence fewer grid points are needed to approximate these smaller gradients. To minimize the calculation time, we gradually reduce the number of grid points.

APPENDIX C: TEMPERATURE OVERSHOOT

In this section, we present our observations on the temperature overshoot based on our numerical simulation of the equilibration process under normal gravity. We find that stratification plays an important role in equilibration for $\epsilon<1\times10^{-3}$. More studies are needed in order to fully understand the mechanism.

Here we deal with the spatial and temporal variations of the temperature inside the fluid after the step ΔT. First, the thermal diffusivity is higher at the cell bottom than at the cell top; in the early stage of the equilibration, the boundary layer expands faster and more adiabatic energy is drawn at the bottom than at the top. Second, the conversion of adiabatic energy into internal energy varies across the bulk fluid due to the density dependence of the pressure coefficient $(\partial P/\partial T)_\rho$ in Eq. (2). Hence, even the spatially homogeneous δP_0 produces an inhomogeneous temperature profile which causes the temperature at the top to approach the equilibrium ahead of the bottom one. The stronger the stratification, the larger spatial variation will be for the pressure coefficient. Then the piston effect in turn causes a stronger spatial gradient in temperature. This phenomenon is very clearly demonstrated when the stratification becomes nonlinear in space. Then the spatial temperature variation follows that of $(\partial T/\partial P)_\rho$. Since the piston effect pushes the average temperature towards the final equilibrium value, the temperature within the top boundary layer starts overshooting the boundary value $\Delta\epsilon$ at the time of $50t_g-100t_g$. After the overshooting node moves out of the top boundary layer, the heat flux at the top boundary is higher than at the bottom. The whole fluid system then starts to release some extra thermal energy absorbed earlier via the piston effect. The local amplitude of the overshooting reaches a peak and then decays. The motion and final equilibrium location of the node seem to depend on the difference of the thermal diffusivity at the boundaries, and they are very different for fluids with average densities of $\pm\Delta\rho\neq0$. The whole fluid system approaches final equilibrium with a single relaxation time only after the node motion is negligible.

The density equilibration with stratification is even more complicated to describe than that of the temperature. It is affected by the temperature overshoot and spatial variation of the thermal expansion coefficient and compressibility. The density also overshoots its final equilibrium value, but it is not always driven by the temperature overshoot.

APPENDIX D: ONSET OF CONVECTION NEAR THE CRITICAL POINT

Consider a fluid between two parallel solid boundaries separated by a distance l, with a temperature difference ΔT. The control parameter for convection is the Rayleigh number

$$R\equiv\frac{g\alpha_P l^3\Delta T}{\nu D_T}, \tag{D1}$$

where ν is the kinematic viscosity (η/ρ) and α_P is the isobaric thermal expansion coefficient. When the fluid compressibility is neglected, we have the Rayleigh criterion for the onset of convective instability, namely, $R<\gamma_0$ results in no convection and $R>\gamma_0$ causes convection. Here γ_0 is a number with the value 1708 for solid boundaries [36]. This criterion does not apply for a fluid near the critical point, where the compressibility diverges. Gitterman and Steinberg [37,38] have developed an expression for the critical Rayleigh number to describe the onset of convective instability near the critical point, and obtain

$$R_c=\gamma_0\frac{1+(l/l_1)^4+(l/l_1)^2(l_2/l_1)^2}{1+(l_3/l_1)^4(l_2/l)^2}, \tag{D2}$$

where

$$l_1 = \left[\gamma_0 \nu D_T \Big/ g^2 \left(\frac{\partial \rho}{\partial P} \right)_T \left[1 - \frac{C_V}{C_P} \right] \right]^{1/4}, \quad \text{(D3a)}$$

$$l_2 = \left[\frac{\gamma_1 \nu D_T}{1 - C_V/C_P} \left(\frac{\partial \rho}{\partial P} \right)_T \right]^{1/2}, \quad \text{(D3b)}$$

$$l_3 = \left[\frac{\gamma_0 \nu D_T}{g^2 (\partial \rho / \partial P)_T} \right]^{1/4}. \quad \text{(D3c)}$$

Equations (D2) and (D3) are derived without consideration of the density stratification. We have used Eqs. (D1) and (D2) to calculate the critical temperature difference $|\Delta T_c|$ across a fluid layer of ^{3}He at the critical isochore for the onset of convection. For our experimental setup, both solid boundaries are at the same temperature which undergoes a steplike change by ΔT to a new value. For $\Delta T > 0$, the heat goes into the fluid layer from both the top and the bottom boundaries; but only the bottom half of the fluid will be mechanically unstable. As a result we use the boundary condition of solid bottom surface and free top surface with $l = h/2 = 0.21$ cm. With this boundary condition [39], $\gamma_0 = 1100.657$ and $\gamma_1 = 70.5$. (Reference [39] does not give γ_1 for the boundaries we choose, so we use the value of γ_1 for both boundaries being solid surfaces.) The known properties of ^{3}He are used in the calculation. The result is shown in Fig. 22 where $\Delta T_{\text{conv. onset}}$ is plotted logarithmically as a function of ϵ along the critical isochore. Here, unlike for an incompressible fluid where $|\Delta T_{\text{conv. onset}}|$ continues to decrease sharply as T_c is approached, the critical temperature difference passes through a shallow minimum and tends to a constant value of $\Delta T = 7.2\ \mu$K.

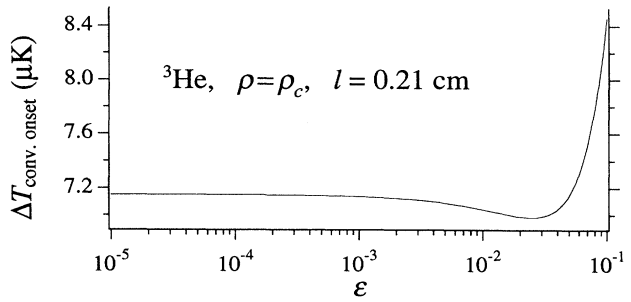

FIG. 22. The temperature difference ΔT for the onset of convection in ^{3}He with effective cell height of 0.21 cm, plotted versus ϵ along the critical isochore.

In our experiment described in Sec. IV, the temperature steps did produce initial temperature differences in excess of this limiting value. However, we have seen only very limited evidence of convection effects. There are three possibilities. First, Gitterman and Steinberg [37] have discussed the influence of density stratification on the predicted ΔT_c and found that it increases strongly as a function of l. Second, the temperature difference between the interior and boundaries is quickly reduced by the piston effect in seconds and does not exceed ΔT_c through the transient stages. Third, it is also conceivable that the geometry inside our cell causes a smaller length scale l than $h/2$, and therefore a larger ΔT can be sustained before convection sets in. In our experiments we have not conducted a search for the critical $\Delta T_{\text{conv. onset}}$.

[1] J. Straub and K. Nitsche (unpublished).

[2] H. Klein, G. Schmitz, and D. Woermann, Phys. Rev. A **43**, 4562 (1991).

[3] See, for instance, R. A. Wilkinson, R. F. Berg, M. R. Moldover, L. Eicher, J. Straub, and R. W. Gammon, in *Proceedings of the VIII European Symposium on Materials and Fluid Sciences in Microgravity, Brussels, Belgium, 1992,* edited by B. Kaldeich (European Space Agency Publication Division, Estec, Postbus 299, 2200 AG, The Netherlands, 1992).

[4] P. Guenoun, B. Khalil, D. Beysens, Y. Garrabos, F. Kammoun, B. Le Neindre, and B. Zappoli, Phys. Rev. E **47**, 1531 (1993).

[5] H. L. Swinney and D. L. Henry, Phys. Rev. A **8**, 2586 (1973).

[6] C. Pittman, L. H. Cohen, and H. Meyer, J. Low Temp. Phys. **46**, 115 (1982), and references therein.

[7] C. Pittman, T. Doiron, and H. Meyer, Phys. Rev. B **20**, 3678 (1979), and references therein.

[8] J. M. H. Levelt Sengers, W. L. Greer, and J. V. Sengers, J. Phys. Chem. Ref. Data **5**, 1 (1976).

[9] J. V. Sengers and J. M. H. Levelt Sengers, in *Progress in Liquid Physics,* edited by C. A. Croxton (Wiley, New York, 1978), p. 103.

[10] J. V. Sengers, R. S. Basu, and J. M. H. Levelt Sengers, NASA Contractor Report No. 3424, 1981 (unpublished).

[11] F. Zhong and H. Meyer (unpublished).

[12] F. Zhong and H. Meyer, J. Am. Soc. Mech. Eng. **AMD-174**, 139 (1993).

[13] F. Zhong and H. Meyer, in *Proceedings of NASA/JPL 1994 Microgravity Low Temperature Physics Workshop, 1994, Washington, D.C.,* National Aeronautics and Space Administration Report No. JPL D-11775, p. 62.

[14] F. Zhong and H. Meyer, in *Proceedings of the NASA/JPL 1994 Microgravity Low Temperature Physics Workshop, 1994, Washington, DC* [13], p. 73.

[15] F. Zhong and H. Meyer, in *Proceedings of the 12th Symposium on Thermophysical Properties, NIST, Boulder, CO, 1994,* edited by J. M. H. Levelt Sengers (Plenum, New York, in press).

[16] A. Onuki and R. A. Ferrell, Physica A **164**, 245 (1990).

[17] H. Boukari, J. N. Shaumeyer, M. E. Briggs, and R. W. Gammon, Phys. Rev. A **41**, 2260 (1990).

[18] H. Boukari, R. L. Pego, and R. W. Gammon (unpublished).

[19] A. Onuki, H. Hao, and R. A. Ferrell, Phys. Rev. A **41**, 2256 (1990).

[20] D. B. Roe and H. Meyer, J. Low Temp. Phys. **30**, 91 (1978).

[21] R. A. Ferrell and H. Hao, Physica A **197**, 23 (1993).

[22] See, for instance, W. H. Press, B. P. Flannery, S. A. Teukolsky, and W. T. Vetterling, *Numerical Recipes in C, the*

Art of Scientific Computing (Cambridge University Press, Cambridge, England, 1991).
[23] R. F. Berg, Phys. Rev. E **48**, 1779 (1993).
[24] J. Straub and K. Nitsche, Fluid Phase Equil. **88**, 183 (1993).
[25] J. Straub, L. Eicher, and A. Haupt, Int. J. Thermophys. (to be published).
[26] J. Straub and A. Haupt, Int. J. Thermophys. (to be published).
[27] H. Boukari, Ph.D. thesis, University of Maryland, 1990.
[28] R. P. Behringer, A. Onuki, and H. Meyer, J. Low Temp. Phys. **81**, 71 (1990).
[29] H. Meyer, in *Measurement of the Transport Properties of Fluids, Experimental Thermodynamics,* edited by W. A. Wakeham, A. Nagashima and J. V. Sengers (Blackwell Scientific Publications, Oxford, 1990), Vol. III, p. 391.
[30] M. G. Ryschkewitsch and H. Meyer, J. Low Temp. Phys. **35**, 103 (1979).
[31] R. G. Brown and H. Meyer, Phys. Rev. A **6**, 364 (1972).
[32] R. P. Behringer, T. Doiron, and H. Meyer, J. Low Temp. Phys. **24**, 35 (1976).
[33] C. C. Agosta, S. Wang, L. H. Cohen, and H. Meyer, J. Low Temp. Phys. **67**, 237 (1987).
[34] J. V. Sengers, in *Transport Phenomena,* edited by J. Kestin AIP Conf. Proc. No. 11 (AIP, New York, 1973), p. 229.
[35] J. F. Thompson, Z. U. A. Warsi, and C. W. Mastin, *Numerical Grid Generation* (North-Holland, New York, 1985), Chap. 8.
[36] L. D. Landau and E. M. Lifshits, *Fluid Mechanics,* Course in Theoretical Physics Vol. 6 (Pergamon, Oxford, 1987).
[37] M. Gitterman and V. A. Steinberg, Teplofiz. Vys. Temp. **8**, 799 (1970) [High Temp. USSR **8**, 754 (1971)].
[38] M. Gitterman and V. A. Steinberg, Prikl Mat. Mekh. **34**, 325 (1970) [J. Appl. Math. Mech. USSR **34**, 305 (1979)].
[39] M. Gitterman, Rev. Mod. Phys. **50**, 85 (1978).